Molecular Mechanics for Chemical Reactions: A Standard Strategy for Using Multiconfiguration Molecular Mechanics for Variational Transition State Theory with Optimized Multidimensional Tunneling

Titus V. Albu, José C. Corchado, and Donald G. Truhlar*

Department of Chemistry and Supercomputer Institute, University of Minnesota, Minneapolis, Minnesota 55455-0431

Received: May 22, 2001; In Final Form: July 10, 2001

Multiconfiguration molecular mechanics (MCMM) is an extension of molecular mechanics to chemically reactive systems. This dual-level method combines molecular mechanics potentials for the reactant and product configurations with electronic structure Hessians at the saddle point and a small number of nonstationary points to model the potential energy surface in the reaction swath region between reactants and products where neither molecular mechanics potential is valid. The resulting semiglobal potential energy surface is used as input for dynamics calculations of tunneling probabilities and variational transition state theory rate constants. In this paper, we present a standard strategy for applying MCMM to calculate rate constants for atom transfer reactions. In particular, we propose a general procedure for determining where to calculate the electronic structure Hessians. We tested this strategy for a diverse test suite of six reactions involving hydrogen-atom transfer. It yields reasonably accurate rate constants as compared to direct dynamics using an uninterpolated full potential energy surface at the same electronic structure level. Furthermore, the rate constants at each of several successively more demanding levels of dynamical theory are also predicted accurately, which indicates that the MCMM potential energy surface accurately predicts many different details of the potential energy surface with a limited number of electronic structure Hessians.

1. Introduction

Variational transition state theory with multidimensional tunneling contributions (VTST/MT) is a powerful method for studying chemical reaction dynamics.[1−6] Its accuracy is mainly limited by the level of electronic structure theory used for the potential energy surface (PES) underlying the dynamics. For medium- and large-sized systems, it is usually prohibitively difficult to obtain an analytic PES so one employs direct dynamics,[7−32] which is the calculation of dynamical quantities or rate constants directly from electronic structure calculations of the energy and forces without the intermediacy of an analytic potential energy function. In recent years, electronic structure methods have reached a high level of accuracy;[33−43] the use of the most accurate of these methods, though, is still prohibitively expensive for direct dynamics methods for large and very large systems, especially when the critical region of the PES is delocalized. When the critical region of the PES is delocalized, either due to variational effects (which result from the variational transition state or dynamical bottleneck not being at the saddle point) or due to tunneling, these calculations require a large number of energy, gradient, and Hessian calculations along the reaction path and sometimes in the corner-cutting-tunneling region of the reaction swath[12,44−50] as well. The reaction swath is defined as the union of the narrow valley centered along the minimum energy path (MEP) and the wider region on the concave side of the MEP that is associated with large-curvature tunneling (i.e., extensive nonclassical corner cutting). Progress may be advanced by developing new and reliable algorithms that yield good accuracy from a small number of electronic structure calculations. The refinement of such algorithms will allow the calculation of rate constants including important dynamical effects with a minimal computational effort. In this way, one can treat a wide variety of reactions with advanced levels of electronic structure theory and thereby obtain more reliable results.

Several algorithms for interpolating potential energy information along the reaction path or in the reaction swath have been proposed in the recent literature.[51−62] Our focus in the present paper is on those especially designed for the efficient calculation of rate constants. One of them, the interpolated variational transition-state theory by mapping (IVTST-M) algorithm,[58] uses electronic data (energy, gradients, and Hessians) computed at a small number of points along the MEP. These data is fitted to splines under tension as functions of a mapped independent variable that depends nonlinearly on the reaction coordinate. Reasonable accuracy in calculated rate constants, including small-curvature corner-cutting tunneling paths, was obtained for the investigated test cases with less than a hundred gradients and less than ten Hessians calculations at nonstationary points.[58] The method does not, however, allow the calculation of the large-curvature corner-cutting tunneling contributions that have been found to contribute significantly for some reactions. Another algorithm, called VTST with interpolated corrections (VTST-IC),[54,61] allows for dual-level interpolations in the large-curvature-tunneling region of the reaction swath, but so far at least, it has been formulated only without high-level data in the large-curvature tunneling region, and this prevents systematic strategies for improvements of the interpolation in that region by adding more points.

More recently, another efficient algorithm, called multiconfiguration molecular mechanics (MCMM), has been intro-

10.1021/jp011951h CCC: $20.00
Published on Web 08/16/2001

duced.[60] This algorithm may be thought of as a dual-level scheme that uses molecular mechanics potential functions[63−68] as the lower-level data and electronic structure theory as the higher-level data. This is accomplished by forming an electronically nonadiabatic (i.e., diabatic) Hamiltonian matrix **V** whose diagonal elements are given by classical molecular mechanics and whose off-diagonal elements are obtained by Shepard interpolation of quadratic expansions around a set of points where the higher-level electronic structure data is available. Note that the nonadiabatic representation is not unique, but the kind we have in mind here is a valence bond Hamiltonian in which V_{11} is the energy of a valence bond state with the reactant's bonding pattern, V_{22} is the energy of a valence bond state with the product's bonding pattern, and V_{12} is their resonance energy. Such representations have been used in a variety of contexts for modeling reactive systems in the past.[69−107] The MCMM method is actually a general fitting scheme for creating semiglobal PESs for reactive systems, and because a PES is constructed, it is not, strictly speaking, a direct dynamics method at all; however, it accomplishes the main objective of any direct dynamics scheme for VTST/MT calculations in that it allows one to carry out the entire dynamics calculation from a reasonably small amount of electronic structure data without requiring the traditional human judgment associated with the "art" of fitting multidimensional functions. The whole fitting process is unique and automatic with one exception, namely, the decision where to locate the input data. In principle, the results converge to a numerically accurate interpolation of the PES for any reasonable scheme of adding data, but our goal in the present article is to discuss and to use the method not with a numerically converged amount of data, but rather with close to the minimal amount of data that is required to calculate reasonably well converged rate constants. More specifically, our objective in the present paper is to develop a "standard" scheme for locating the data that minimizes the number of points at which data is used and to test this scheme broadly.

In MCMM, the Born−Oppenheimer potential energy surface is obtained as the lowest eigenvalue of the matrix **V**, and it reproduces the higher-level data in the vicinity of each data point. An important feature of the method is that the electronic structure calculations are not required to be on the MEP, and this extends the range of applicability compared to IVTST-M, which uses a large number of gradient calculations to converge the MEP. Accurate rate constants have been achieved with MCMM, even for large-curvature tunneling-dominated reactions, with a very small number of electronic structure Hessians, as low as one Hessian at the saddle point and four Hessians at nonstationary points.[60] By adding more electronic structure data, the results will converge to the same rate constants as computed by a direct dynamics calculations at the higher level.

The first result of this paper is that we report a strategy for converging the potential energy surface in the reaction swath region well enough to calculate accurate rate constants. Then, we test how well calculations based on this strategy, with a limited small number of electronic structure data, reproduce the much more expensive direct dynamics calculation at a given electronic structure level. For such tests, the electronic structure method must be realistic but need not be in quantitative agreement with experiment; in fact (although the ultimate goal is to develop an efficient scheme for predicting experimental observables), comparison with experiment is irrelevant to the present tests. The standard scheme for the MCMM algorithm that is developed in this paper is tested on a set of six hydrogen-transfer reactions. We choose reactions simple enough that we can afford direct dynamics calculations to which the MCMM results will be compared, yet complex enough that there are 2, 11, 14, 17, 20, and 33 vibrational degrees of freedom transverse to the reaction path. The test suite used here presents challenges in determining both variational and tunneling effects, and it includes both cases dominated by small-curvature tunneling and cases dominated by large-curvature tunneling.

2. Overview of the Dynamical Theory

Canonical variational transition-state theory (CVT) with semiclassical multidimensional tunneling contributions is used for the dynamics calculations.[1−6,12,14,16−20,23,44−50,108−114] The transmission coefficients are calculated using the zero-curvature tunneling (ZCT) approximation,[16,111,114] the centrifugal-dominant small-curvature semiclassical adiabatic ground-state tunneling (called small-curvature tunneling or SCT) approximation,[16,17] version 4 of the large-curvature tunneling (LCT) approximation,[16,18,19,44−48,50,114] and the microcanonical optimized multidimensional tunneling (μOMT) approximation.[18,114] The LCT result includes tunneling into vibrationally excited states. It is also of interest to consider the result obtained if we use the large-curvature tunneling approximation but only allow tunneling into the ground vibrational state; this is called LCT(0). The μOMT result is obtained by selecting, for any total energy, the larger of the SCT and LCT probabilities. In calculating the tunneling coefficients, we also include the nonclassical reflection at energies above the classical barrier to account for quantum effects on reaction-coordinate motion.[108]

The canonical variational transition-state theory rate constant, k^{CVT}, is obtained by variationally minimizing the generalized transition-state rate constant, k^{GT}, with respect to the position s of the generalized transition state along the reaction coordinate[3−5,111,112]

$$k^{CVT}(T) = \min_{s} k^{GT}(T, s) \tag{1}$$

where the reaction coordinate s is the signed distance along the minimum energy path in the isoinertial coordinate system[3113] in which all coordinates are scaled to a common reduced mass μ. Note that s has a negative value on the reactant side of the saddle point and a positive value on the product side. The conventional transition-state theory (TST) rate constant, k^{TST}, is obtained for $s = 0$ (the saddle point). Any deviation of k^{CVT} from k^{TST} is called a variational effect.

The tunneling calculation is based in part on $V_a^G(s)$, which is the vibrationally adiabatic ground-state potential energy curve defined, for nonlinear systems, as

$$V_a^G(s) = V_{MEP}(s) + \sum_{m=1}^{3N_{atoms}-7} \frac{1}{2}\hbar\omega_m(s) \tag{2}$$

where $\omega_m(s)$ is the frequency of generalized normal mode m at location s along the MEP, and N_{atoms} is the total number of atoms in the reactive system. It is convenient to define for each reactive system a high side and a low side based on the relative energy of V_a^{RG} and V_a^{PG}, which are the reactant and product values of $V_a^G(s)$. (For a bimolecular reaction, these are asymptotic values). If $V_a^{RG} > V_a^{PG}$, we define the high side of a reactive system to be the reactant side of the saddle point (negative s) and the low side to be the product side of the saddle point (positive s). In this case, we denote V_a^{RG} as V_a^{HG}, and V_a^{PG} as V_a^{LG}. Similarly, if $V_a^{PG} > V_a^{RG}$ the high side is the product side (V_a^{PG} becomes V_a^{HG}) and the low side is the reactant side (V_a^{RG}

becomes V_a^{LG}). The rate constant including tunneling is then given by

$$k^{CVT/MT} = \kappa^{MT} k^{CVT} \quad (3)$$

where κ^{MT} is the transmission coefficient (it would be $\kappa^{CVT/MT}$ in the notation of ref 111), and MT is ZCT, SCT, LCT(0), LCT, or μOMT. The transmission coefficient is given by[111]

$$\kappa^{MT} = \int_{V_a^{HG}}^{\infty} d(E/RT) P^{MT}(E) \exp\{-[E - V_a^G(s_*^{CVT}(T))]/RT\} \quad (4)$$

where $P^{MT}(E)$ is the ground-state tunneling probability at energy E, $s_*^{CVT}(T)$ is the location of the dynamical bottleneck at T, and R is the gas constant. In CVT/MT calculations, the tunneling contributions are always calculated from the ground state of the high side to the ground and excited states of the low side. For interpretative purposes, it is sometimes useful to calculate the representative tunneling energy (E_{rep}). This is defined as the energy at which the integrand of eq 4 is a maximum when MT is μOMT, unless this maximum occurs at an energy above the maximum of V_a^G, in which case E_{rep} is set equal to this value.

We note that it is important to converge the SCT calculation even when LCT is dominant and to converge LCT even when SCT is dominant; otherwise, one does not know reliably which one is larger and therefore dominant.

3. Review of Multiconfiguration Molecular Mechanics

The MCMM algorithm[60] provides an approximate multidimensional PES by combining a limited number of higher-level data (energies, gradients, and Hessians) with molecular mechanics[63−68] potentials. The constructed PES may be used for studying the dynamics of reactive systems. MCMM is essentially a combination of four computational techniques: (i) the empirical valence bond method,[69−75,77,85,87,88,93,98,104] (ii) Chang, Minichino, and Miller's method of estimating V_{12} in empirical valence bond calculations,[86,91] (iii) the use of redundant internal coordinates to represent low-order expansions of potential energy surfaces in internal coordinates,[22,115,116] and (iv) the Shepard interpolation method.[55,56] The method may also be considered as a special case of the general idea that because the lowest PES of a polyatomic system emerges actually as the lowest eigenvalue of a very large configuration interaction matrix, it may be reasonably approximated as the lowest eigenvalue of a small matrix.[117] A full treatment of the algorithm is presented in the original paper;[60] here, we present just a summary.

The Born−Oppenheimer potential energy is represented at any geometry defined in internal coordinates $\mathbf{q}$ as the lowest eigenvalue of a 2×2 electronically diabatic Hamiltonian matrix $\mathbf{V}$

$$\mathbf{V} = \begin{pmatrix} V_{11}(\mathbf{q}) & V_{12}(\mathbf{q}) \\ V_{12}(\mathbf{q}) & V_{22}(\mathbf{q}) \end{pmatrix} \quad (5)$$

where the V_{11} and V_{22} elements are taken as classical molecular mechanics potential functions that describe reactant and product valence bond configurations. The V_{12} element is called the resonance energy function or the resonance integral. The lowest eigenvalue is

$$V(\mathbf{q}) = \frac{1}{2}\{(V_{11}(\mathbf{q}) + V_{22}(\mathbf{q})) - [(V_{11}(\mathbf{q}) - V_{22}(\mathbf{q}))^2 + 4V_{12}(\mathbf{q})^2]^{1/2}\} \quad (6)$$

The first and second derivatives of V (which is the information required for the dynamical calculations) are obtained by differentiation of eq 6. The molecular mechanics potentials V_{11} and V_{22} are readily available, inexpensive to calculate, and "easy" to differentiate analytically. The resonance integral V_{12} and its derivatives are the key features of the MCMM algorithm, and they are obtained using Shepard interpolation.[55,56] In this interpolation algorithm, we use a set of M points called Shepard points $\mathbf{q}^{(k)}$ at which we have the energies $V^{(k)}$, gradients $\mathbf{g}^{(k)}$, and Hessian matrices $\mathbf{f}^{(k)}$ from electronic structure calculations, where $k = 1, 2, ..., M$. This yields an expansion of V in a Taylor's series around geometry $\mathbf{q}^{(k)}$, and we use molecular mechanics to expand V_{11} and V_{22}. Then, using eq 6, we obtain a quadratic expansion of V_{12} around point $\mathbf{q}^{(k)}$. This quadratic expansion, which is transformed in internal coordinates[60] to avoid any ambiguity[118] of the system orientation in space, is called $V_{12}(\mathbf{q}; k)$.

Each of these quadratic expansions is completely determined by an electronic structure calculation of the energy, gradient, and Hessian at that point. As before,[60] we obtain V_{12} at other geometries by means of Shepard interpolation in internal coordinates, as a linear combination of the quadratic expansions around the Shepard points

$$V_{12}^S(\mathbf{q}) = \sum_{k=1}^{M} W_k(\mathbf{q}) V'_{12}(\mathbf{q}; k) \quad (7)$$

where $W_k(\mathbf{q})$ are normalized weights, and $V'_{12}(\mathbf{q}; k)$ is a modified quadratic function

$$V'_{12}(\mathbf{q}; k)^2 = [V_{12}(\mathbf{q}; k)]^2 u(\mathbf{q}; k) \quad (8)$$

and the modification is[60]

$$u(\mathbf{q}; k) = \begin{cases} \exp\{-\delta/[V_{12}(\mathbf{q}; k)]^2\} & [V_{12}(\mathbf{q}; k)]^2 > 0 \\ 0 & [V_{12}(\mathbf{q}; k)]^2 \le 0 \end{cases} \quad (9)$$

with $\delta = 1 \times 10^{-8}\ E_h^2$ (note: $1E_h = 1$ hartree $= 627.51$ kcal/mol).

We used the same functional form for the normalized weights as in the original MCMM study[60]

$$W_k(\mathbf{q}) = \left(\frac{1}{d_k(\mathbf{q})}\right)^4 \Big/ \sum_{i=1}^{M} \left(\frac{1}{d_i(\mathbf{q})}\right)^4 \quad (10)$$

where $d_k(\mathbf{q})$ denotes a generalized distance between $\mathbf{q}$ and $\mathbf{q}^{(k)}$ that is defined as

$$d_k(\mathbf{q}) = \sqrt{\sum_{j=1}^{j_{max}} (q_j - q_j^{(k)})^2} \quad (11)$$

Various strategies for the MCMM calculations may differ in the number and the choice of internal coordinates used to calculate the generalized distance. In this study, the internal coordinates used to calculate the generalized distance in eq 11 are three interatomic distances that change significantly during reaction. In all calculations in the present paper, we use the forming bond distance, the breaking bond distance, and the distance between the nontransferring atoms involved in these bonds. Therefore, $j_{max} = 3$. For example, for a reaction of type:

$$CA + H{-}BD \rightarrow CA{-}H + BD \quad (12)$$

where "−" denotes a bond, the generalized distance is calculated

as

$$d_k(\mathbf{q}) = \sqrt{[r_{AH}(\mathbf{q}) - r_{AH}(\mathbf{q}^{(k)})]^2 + [r_{BH}(\mathbf{q}) - r_{BH}(\mathbf{q}^{(k)})]^2 + [r_{AB}(\mathbf{q}) - r_{AB}(\mathbf{q}^{(k)})]^2} \quad (13)$$

All M points used in Shepard interpolation should include all atoms of the reactive system. This is straightforward for a unimolecular reaction that produces a single product; however, the present paper considers bimolecular reactions with two products. For a bimolecular reaction, the $k = 1$ point is always a bound complex (e.g., a van der Waals complex or an ion−dipole complex). Similarly, the $k = 2$ point would be the product if there were only one product, but it is a well in the product valley, or a bound complex for a reaction yielding two products. The $k = 3$ point is the saddle point. This is the minimum number of points for Shepard interpolation in the MCMM algorithm. Besides these points, we also use an additional number of points $k = 4, ..., M$. The additional points are called supplementary points and they are labeled $\alpha = 1, 2, ..., N_s$ where $\alpha = k - 3$. In this notation, the saddle point is called $\alpha = 0$. It should be pointed out that the method uses molecular mechanics information for the reactant-valley well and the product-valley well ($k = 1, 2$). The number of points at which the higher-level electronic structure information is used for Shepard interpolation is $N_s + 1$ (or $M - 2$). For the $N_s + 1$ points used for Shepard interpolation the algorithm requires an energy, gradient, and Hessian. We also carry out electronic structure calculations for the reactants and products themselves. The reactant and product electronic structure energies are also used for determining the zero of energy of V_{22} relative to V_{11}. We also require the Hessian for the reactant in order to compute its partition function, and we require Hessians for both reactants and products for the tunneling calculations.

The notation for MCMM rate constants is based on the number of supplementary points used in a given calculation; in particular, we use the notation MCMM−N_s. For example, MCMM−4 means that we are using $N_s = 4$ (which corresponds to $M = 7$) for the Shepard interpolation.

4. Standard Strategy for Multiconfiguration Molecular Mechanics

There are various possible strategies for using the MCMM algorithm depending on the functional form used for the normalized weights and on the locations of the electronic structure data. We consider that eq 10 is an important part of the algorithm (the functional form of eq 10 was carefully optimized in ref 60), but the choice of j_{max}, the choice of which coordinates to use in eq 11, and the locations of the data points need further discussion. In the present study we compared $j_{max} = 2$ (the two internal coordinates considered were the breaking bond distance and the making bond distance) to $j_{max} = 3$ and found that $j_{max} = 3$ works much better. Thus, in the present paper all results are based on eq 13. The final issue then is data point placement. As stated in the Introduction, an important goal of this paper is to propose a standard set of locations for adding the supplementary points. The MCMM rate constants and potential energy surface depend on the number and location of the Shepard points. By adding more points, the MCMM results would eventually converge to the uninterpolated direct dynamics ones, i.e., to straight direct dynamics. There are many ways of selecting the locations of the Shepard points, and we found that it is easier to develop a good scheme for a single system than to develop a scheme that works well when used without modification for several systems. Our goal is to obtain good results for all reactions in our test suite with a single, general scheme using as small an amount of higher-level data of possible.

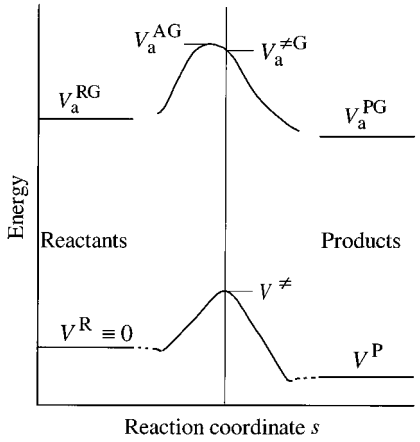

Figure 1. Schematic representation of the potential energy and the vibrationally adiabatic ground-state energy along the minimum energy path, and the definition of the values of these quantities for the reactants (V^R and V_a^{RG}), the products (V^P and V_a^{GP}), the saddle point ($V^{\neq}$ and $V_a^{\neq G}$), and the dynamical bottleneck at 0 K (V_a^{AG}).

In the process of selecting the locations of the electronic structure Hessian for point α we always take advantage of the information along the MEP as determined in the MCMM−($\alpha - 1$) calculation. We consider both the potential energy surface along the minimum energy path, $V_{MEP}(s)$, and the vibrationally adiabatic ground-state potential energy curve, $V_a^G(s)$. We take into account the values at the reactants, the products, and the saddle point denoted V^R, V^P, and $V^{\neq}$ for $V_{MEP}(s)$, and denoted V_a^{RG}, V_a^{PG}, and $V_a^{\neq G}$ for $V_a^G(s)$. The values of these quantities are determined by electronic structure calculations and do not depend on the MCMM algorithm. A schematic representation of these quantities is given in Figure 1. We also sometimes discuss the maximum of the $V_a^G(s)$ curve, which corresponds to the dynamical bottleneck at 0 K, and its location along the MEP; these are denoted V_a^{AG} and s_*^{AG} respectively, and they depend on the sequence number α in the MCMM−α calculations. We define V^R as the overall zero of energy for each system, and thus all $V_{MEP}(s)$ and $V_a^G(s)$ values are with respect to that zero of energy.

We locate the Shepard points in a way that is not dependent on the direction in which a reaction is investigated. Thus, we use the definition of high side and low side introduced in section 2. (For the reactions investigated in this paper, the $V_a^{RG} > V_a^{PG}$ condition is also equivalent to $V^R > V^P$, but that need not be the case in general.) We define the intrinsic barrier height (IBH) as the difference between $V^{\neq}$ and potential energy of the high side. Therefore, the IBH is equal to $V^{\neq}$ if the reactant side is the high side and is equal to ($V^{\neq} - V^P$) if the product side is the high side. In addition to distinguishing the high and low sides, we distinguish the dynamical bottleneck side at 0 K, which is the side on which s_*^{AG} occurs. For simplicity, we will just call the dynamical bottleneck side without mentioning 0 K every time.

In the standard sequence, the first dynamics calculation performed is based on the MCMM−0 surface, which is constructed using the molecular mechanics information from the reactant-valley well ($k = 1$) and the product-valley well ($k = 2$), and electronic structure information at the saddle point

($\alpha = 0$). The first supplementary point ($\alpha = 1$) is taken to be along the MEP of the MCMM−0 run, lower than saddle point by an energy equal to $^1/_4$ of the IBH, on the dynamical bottleneck side of the MCMM−0 calculation. In practice, we choose the closest point on a 0.01 a_0 grid along the MEP, and this is true for the following points also. The calculation with these four Shepard points is called MCMM−1 because it involves only one supplementary point. The second supplementary point ($\alpha = 2$) is taken to be along the MEP of the MCMM−1 run, lower than saddle point by $^1/_4$ of the IBH, on the side of the saddle point opposite to the $\alpha = 1$ point. This calculation is called MCMM−2. The third supplementary point ($\alpha = 3$) is taken to be along the MEP of the MCMM−2 run, lower than saddle point by $^1/_2$ of the IBH, on the dynamical bottleneck side of the MCMM−2 run. This calculation is called MCMM−3. The fourth supplementary point ($\alpha = 4$) is taken to be along the MEP of the MCMM−3 run, lower than saddle point by $^1/_2$ of the IBH, on the side of the saddle point opposite to the $\alpha = 3$ point. This calculation, with seven Shepard points, is called MCMM−4.

The fifth supplementary point ($\alpha = 5$) is taken to be along the MEP of the MCMM−4 run, on the dynamical bottleneck side. Its energy depends on whether the dynamical bottleneck is on the high side or on the low side of the saddle point. The $\alpha = 5$ point is taken lower than saddle point by $^3/_4$ of the IBH if the high side is the dynamical bottleneck side or lower than saddle point by $^3/_4$ of the average of forward and backward barrier heights if the low side is the dynamical bottleneck side. This calculation, with eight Shepard points, is called MCMM−5.

The sixth supplementary point ($\alpha = 6$) is taken to be along the MEP of the MCMM−5 run, on the dynamical bottleneck side. To understand how we choose its location, one should recall that six other points (including the saddle point) were already placed on the MEP (although some of them are on MEPs calculated in earlier stages and, hence, not precisely on the current best estimate of the MEP). These six points define five intervals; the $\alpha = 6$ point is chosen in whichever of these intervals contains the MCMM−5 dynamical bottleneck. The energy of the $\alpha = 6$ point is taken to be lower than the saddle point by $^1/_8$ of IBH if the dynamical bottleneck is between the $\alpha = 1$ and $\alpha = 2$ points, $^3/_8$ of IBH if the dynamical bottleneck is between an $\alpha = 1$ or 2 point and an $\alpha = 3$ or 4 point, or $^5/_8$ of the IBH if the dynamical bottleneck is between an $\alpha = 3$ or 4 point and $\alpha = 5$ point. This calculation, with nine Shepard points, is called MCMM−6.

The seventh supplementary point ($\alpha = 7$) is taken to be along the MEP of the MCMM−6 run, on the side of the saddle point opposite to the $\alpha = 5$ point. The energy of the $\alpha = 7$ point is taken lower than saddle point by $^3/_4$ of the IBH if the $\alpha = 7$ point is on the high side or lower than saddle point by $^3/_4$ of the average of forward and backward barrier heights if the $\alpha = 7$ point is on the low side. This calculation, with ten Shepard points, is called MCMM−7.

The eighth supplementary point ($\alpha = 8$) is not taken along the MEP, but rather on the concave side of the reaction path. This point is located halfway along the line in Cartesian coordinates that connects a point on the high side whose $V_a^G(s)$ is equal to $0.50V_a^{HG} + 0.50V_a^{\ddagger G}$ with a point on the low side whose $V_a^G(s)$ is equal to $0.50V_a^{LG} + 0.50V_a^{\ddagger G}$. This calculation, with 11 Shepard points, is called MCMM−8.

The ninth supplementary point ($\alpha = 9$) is also on the concave side of the reaction path. This point is located along the line in Cartesian coordinates that connects a point on the high side of the MCMM−8 path whose $V_a^G(s)$ equals $0.75V_a^{HG} + 0.25V_a^{\ddagger G}$ with a point on the low side whose $V_a^G(s)$ equals $0.75V_a^{LG} + 0.25V_a^{\ddagger G}$, one-quarter of the way starting from the high side. This calculation, with 12 Shepard points, is called MCMM−9. Similarly, the tenth supplementary point ($\alpha = 10$) is taken on the concave side of the reaction path, located along the line in Cartesian coordinates that connects a point on the high side of the MCMM−9 path whose $V_a^G(s)$ is $0.75V_a^{HG} + 0.25V_a^{\ddagger G}$ with a point on the low side whose $V_a^G(s)$ is $0.75V_a^{LG} + 0.25V_a^{\ddagger G}$, one-quarter of the way starting from the low side. This calculation, with 13 Shepard points, is called MCMM−10.

5. Systems

In the present study, the MCMM algorithm was tested on six hydrogen-transfer reactions

$$Cl + HBr \rightarrow HCl + Br \quad \text{(R-1)}$$

$$O + CH_4 \rightarrow OH + CH_3 \quad \text{(R-2)}$$

$$OH + CH_4 \rightarrow H_2O + CH_3 \quad \text{(R-3)}$$

$$NH_2 + CH_4 \rightarrow NH_3 + CH_3 \quad \text{(R-4)}$$

$$CH_2F + CH_3Cl \rightarrow CH_3F + CH_2Cl \quad \text{(R-5)}$$

$$OH + C_3H_8 \rightarrow H_2O + sec\text{-}C_3H_7 \quad \text{(R-6)}$$

These reactions differ from one another in significant ways, and together they provide a challenging test suite. The number of atoms varies from 3 to 13. We will see below that the classical barrier height varies from 2.7 to 15.7 kcal/mol, and the zero-point-exclusive energy of reaction varies from −16.5 to +7.8 kcal/mol, with two of the reactions being close to thermoneutral. Furthermore, we will see that two of the reactions are dominated by large-curvature tunneling, two are dominated by small-curvature tunneling, and the other two have significant contributions of both small-curvature and large-curvature tunneling. In Table 1 we give the energetic parameters (defined in Figure 1) of the reactive systems investigated here as determined from the electronic structure calculations, and in Table 2 we give information about the bond angle $\theta_{AHB}^{\ddagger}$ at the transferred hydrogen atom at the saddle point, the saddle point distances $r_{AH}^{\ddagger}$ and $r_{BH}^{\ddagger}$, and their comparison to the equilibrium bond distances r_{AH}^{P} and r_{BH}^{R} in products and reactants, respectively.

For the conventional and generalized transition states of reactions R-1 and R-3 to R-6 no low-lying electronically excited states are considered, so the electronic partition is the ground state degeneracy. For reaction R-2, we included only the ground triplet state but treated it as having a degeneracy of 6 to account for the fact that there are two low-lying states that are nearly degenerate. We do include the following electronic excited states in calculating the reactant partition functions: the $^2P_{1/2}$ excited states of Cl with an excitation energy of 881 cm^{-1}, the $^2\Pi_{1/2}$ excited state of OH with an excitation energy on 140 cm^{-1}, and the $^3P_1$ and $^3P_0$ excited states of O(^{3}P) with excitation energies of 158 and 227 cm^{-1} respectively.

6. Computational Details

The MCMM dynamics calculations were carried out using a new version of the TINKERATE[119] computer program that interfaces the POLYRATE[120] and TINKER[121] programs. This version of TINKERATE has the capability of using different internal coordinates for generalized normal-mode analysis along the

TABLE 1: Electronic Structure Energetics for the Systems Investigated[a]

reaction	$V^{\ddagger}$	V^{P}	IBH	V_a^{RG}	V_a^{PG}	$V_a^{\ddagger G}$	V_a^{AG}	s_*^{AG}	E_{rep} (300 K)
$Cl + HBr \rightarrow HCl + Br$[b]	11.89	−9.18	11.89	3.83	−4.82	13.33	13.38	−0.045	10.73
$O + CH_4 \rightarrow OH + CH_3$	13.85	7.81	6.04	28.85	32.55	39.10	39.14	−0.033	35.75
$HO + CH_4 \rightarrow H_2O + CH_3$	7.39	−9.07	7.39	34.41	24.04	40.19	41.27	−0.277	40.46
$NH_2 + CH_4 \rightarrow NH_3 + CH_3$	13.78	−1.97	13.78	41.25	39.52	54.82	54.82	−0.007	48.34
$CH_2F + CH_3Cl \rightarrow CH_3F + CH_2Cl$	15.71	−1.32	15.71	40.47	38.86	54.92	54.92	+0.002	52.09
$HO + C_3H_8 \rightarrow H_2O + sec\text{-}C_3H_7$	2.69	−16.51	2.69	72.21	54.23	73.60	74.58	−0.574	74.58

[a] The $V^{\ddagger}$ is the potential energy at the saddle point (equal to classical forward barrier height), V^{P} is at the products (equal to classical energy of reaction), and IBH is the intrinsic barrier height. The V_a^{RG} is the vibrationally adiabatic ground-state potential energy curve at the reactants, V_a^{PG} is at the products, $V_a^{\ddagger G}$ is at the saddle point, and V_a^{AG} is at the variational transition state (dynamical bottleneck) at 0 K in the direct dynamics calculation. E_{rep} (300 K) is the representative tunneling energy at 300 K; s_*^{AG} is the reaction coordinate at the dynamical bottleneck. By definition the zero of energy for $V^{\ddagger}$, V^{P}, V_a^{RG}, V_a^{PG}, $V_a^{\ddagger G}$, V_a^{AG}, and E_{rep} (300 K) is the classical potential energy at the reactants ($V^{R} \equiv 0$). The s_*^{AG} values are in bohr; all other tabulated values are in kcal/mol. [b] MP2(FC)/6−31G*; all other rows are based on MPW1K/6−31+G(d,p).

TABLE 2: Saddle Point Geometries[a]

reaction	$\theta_{AHB}^{\ddagger}$ (deg)	$r_{AH}^{\ddagger}$ (A)	$r_{BH}^{\ddagger}$ (A)	$r_{AH}^{\ddagger} - r_{AH}^{P}$ (A)	$r_{BH}^{\ddagger} - r_{BH}^{R}$ (A)
$Cl + HBr \rightarrow HCl + Br$[b]	148	1.59	1.57	0.31	0.17
$O + CH_4 \rightarrow OH + CH_3$	179	1.18	1.31	0.22	0.22
$HO + CH_4 \rightarrow H_2O + CH_3$	174	1.28	1.22	0.33	0.13
$NH_2 + CH_4 \rightarrow NH_3 + CH_3$	171	1.26	1.31	0.26	0.22
$CH_2F + CH_3Cl \rightarrow CH_3F + CH_2Cl$	178	1.34	1.33	0.25	0.25
$HO + C_3H_8 \rightarrow H_2O + sec\text{-}C_3H_7$	177	1.41	1.17	0.46	0.08

[a] The hydrogen atom is transferred from B to A according to eq 12. The r_{AH}^{P} is the equilibrium A−H distance in the product, and r_{BH}^{R} is the equilibrium B−H distance in the reactant. [b] MP2(FC)/6−31G*; all other rows are based on MPW1K/6−31+G(d,p).

MEP and for the calculation of the generalized distance $d_k(\mathbf{q})$ in the interpolation step. The direct dynamics calculations were carried out using GAUSSRATE,[122] which is an interface of POLYRATE[120] with Gaussian.[123] All electronic structure calculations were carried out using GAUSSIAN98 software,[123] and all molecular mechanics calculations were carried out with TINKER.

The parameters for the molecular mechanics force field are those of the MM3 force field[64−66] installed in tinker. We needed to define a few molecular mechanics parameters that are not present in the original version of the force field, and these are presented in the Appendix.

The levels of theory used for the electronic structure calculations in this study are MPW1K/6−31+G(d,p) (for reactions R-2 through R-6) and MP2(frozen core)/6−31G(d) (for reaction R-1). Note that 6−31G(d) is also called 6−31G*. MPW1K[43] is a hybrid Hartree−Fock-density functional method[38] that was optimized against a database of barrier heights and reaction energies for 20 reactions, three of which are investigated in the present study (reactions R-2, R-3, and R-4). For the electronic structure calculations, we employed restricted wave functions for closed-shell systems and unrestricted wave functions for open-shell systems.

The results presented in this paper are obtained using the Page−McIver method[124] to follow the MEP in isoinertial coordinates for both the MCMM calculations and the direct dynamics calculations. (We carried out initial studies using the Euler steepest descent algorithm for the direct dynamics calculations, and the results are similar to the Page-McIver results for all but reaction R-6, where Page−McIver algorithm appears to be more stable.) In all cases, the coordinates are scaled to a reduced mass μ of 1 amu. For the direct dynamics calculations, we use a step size of 0.005 a_0 for the gradient, and a Hessian is calculated every 0.05 a_0 along the MEP. For the MCMM calculations, because they are much less expensive, we use a step size for the gradient of 0.001 a_0, and a Hessian is calculated every 0.01 a_0 along the MEP.

For the direct dynamics calculations, the reaction path was calculated out to 2.0 to 4.0 a_0 on the high side and to 2.0 to 3.0 a_0 on the low side. This brings $V_a^G(s)$ 74 to 98% of the way from $V_a^{\ddagger G}$ to its asymptotic value on the low side, V_a^{LG}, and 40 to 99% (40% for R-6 and 73 to 99% for R-1 through R-5) of the way from $V_a^{\ddagger G}$ to V_a^{HG} on the high side. In all cases, this was far enough out to converge the ZCT, SCT, LCT(0), LCT, and μOMT tunneling calculations. LCT and μOMT calculations include tunneling into vibrationally excited states, to the extent that it occurs, and we also report LCT(0) calculations for comparison.

In determining the MCMM rate constants presented here, we apply a systematic criterion in determining the range of s for all six reactions. The end points of these s ranges are always taken on a 0.1 a_0 grid. On the high side, we always use as the end point the first point on the grid past the point where $V_a^G(s)$ equals V_a^{HG}. (Note that $V_a^G(s)$ does not decrease monotonically from V_a^{AG} to V_a^{HG} because of the realistic wells in our surface; the point where $V_a^G(s)$ equals V_a^{HG} is just short of the well.) On the low side, the end point is chosen differently depending on the number of supplementary Shepard points. The end point of the low side is the first point on the grid past the point where $V_a^G(s)$ equals $0.75V_a^{HG} + 0.25V_a^{\ddagger G}$ for MCMM−0 through MCMM−4 calculations, is the first point on the grid past V_a^{HG} for MCMM−5 through MCMM−7 calculations, or is the first point on the grid past $0.95V_a^{LG} + 0.05V_a^{\ddagger G}$ for MCMM−8 through MCMM−10 calculations. The s range as specified above is increased ($0.95V_a^{LG} + 0.05V_a^{\ddagger G}$ is always lower in energy than V_a^{HG} for the cases investigated here) with increases in the number of electronic structure Hessians. The reason for choosing a narrower s range in the MCMM calculations with a small number of electronic structure data is the fact that calculations over the final s ranges sometimes show unphysical behavior of the vibrational normal modes in ranges where the MCMM method is not yet converged. For low values of α the MCMM−α surfaces should be used only in the regions where there is sufficient data. We note that the ranges of s used for MCMM−5 through MCMM−7 are wide enough for converging the ZCT and SCT tunneling calculations, and the ranges for

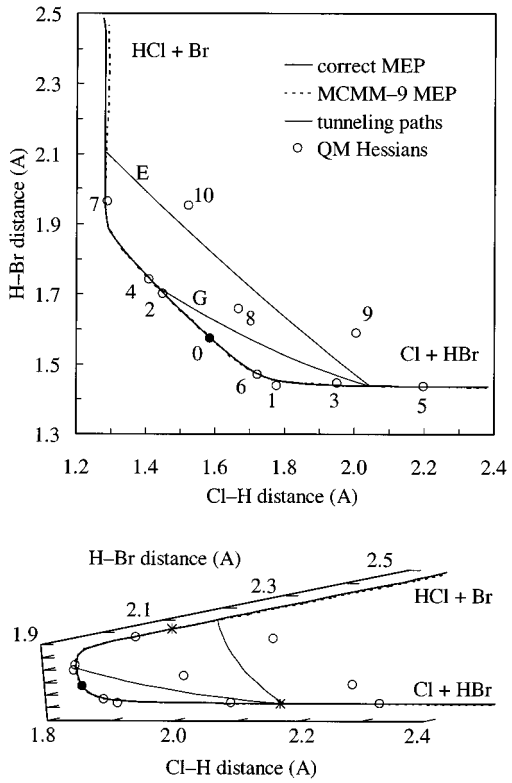

Figure 2. A two-dimensional representation of the reaction path (-1.7 $a_0 < s < +2.0$ a_0) from the MCMM−9 and the direct dynamics calculations, schematics of the MCMM−9 tunneling paths into the ground state (G) and into the first vibrationally excited state (E) at $V_a^G(s)$ equal to $(V_a^{HG} + V_a^{HG})/2$, and the locations of the quantum mechanical (QM) Hessians for the Cl + HBr → HCl + Br reaction. The filled circle represents the saddle point. In the upper panel, the reaction's entrance and exit channels are normal to each other, whereas in the lower panel they are at the skew angle (refs 3 and 114) that correspond to the angle between the entrance and exit valleys in isoinertial coordinates. In the lower panel, the $s = -1.0$ a_0 and $s = +1.0$ a_0 points along the MEP as determined in the direct dynamics calculation are represented by *. The range of the MEP shown in lower panel is identical to that in the upper panel.

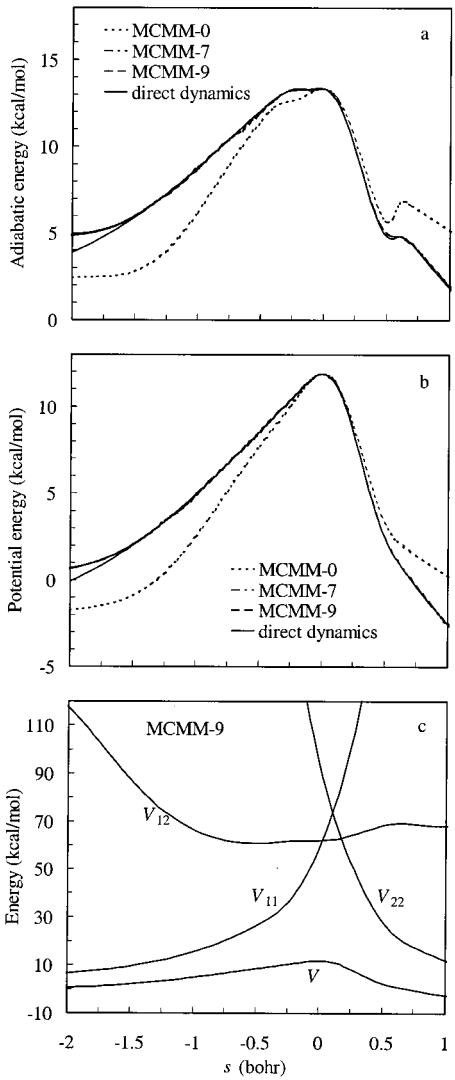

Figure 3. Reaction-path profiles for the Cl + HBr → HCl + Br reaction. (a, b) The vibrationally adiabatic ground-state energies and potential energies along the MEP from calculations with various numbers of supplementary Shepard points and from the direct dynamics calculations. (c) The matrix elements of the electronically diabatic Hamiltonian **V** and the lowest eigenvalue V along the MEP from the MCMM−9 calculation.

MCMM−8 through MCMM−10 are wide enough for converging the ZCT, SCT, LCT(0), LCT, and μOMT tunneling calculations.

In calculating the vibrational partition functions the harmonic approximation is assumed in all cases, and the vibrational analysis is carried out using nonredundant (for R-1) or redundant (for R-2 through R-6) internal coordinates. The internal coordinates used for each case are specified in the Supporting Information. We note that a hindered rotor (rectilinear, single configuration)[125] treatment of the lowest-energy mode for the reactions involving a torsional mode of vibration lowers the partition function calculated with harmonic approximation by less than 50% at the saddle point, at any temperature of interest. Because the purpose of the present study is to compare the calculated MCMM rate constants with direct dynamics rate constants and not to reproduce the experimental values, we decided to use harmonic approximation for all vibrations to avoid complicating the comparison.

It should be noted that, in this study, the choice of redundant or nonredundant internal coordinates used in vibrational normal-mode analysis yields a reaction-path Hamiltonian with all frequencies real along the interesting ranges of the MEP. Accordingly, the IVTST0FREQ option of POLYRATE,[120] an option extensively used in previous CVT studies, has not been used here. This option corresponds to using IVTST−0[52] for the lowest-frequency mode or modes, and not using this option provides an extremely challenging test for the present calculations because the rate constants calculated at low temperatures are very sensitive to the low-frequency vibrational modes.

7. Results

We present the results in Figures 2-16 and Tables 3-9. Figures 2, 4, 6, 8, 10, and 15 show two-dimensional representations of the MEPs calculated at the higher level and by MCMM−9 as well as two-dimensional representations of the locations of the electronic structure data. (We use MCMM−9 runs rather than MCMM−10 to provide a more difficult test of the MCMM algorithm.) For each reaction, we graph the MEPs as functions of the breaking and making bond distances in two representations where the axes are perpendicular to one another and where the axes form a angle equal to the skew angle. The later representation shows the reaction's entrance and exit channels at the same angle as calculated in isoinertial coordinates because the skew angle β is defined as the angle between the entrance

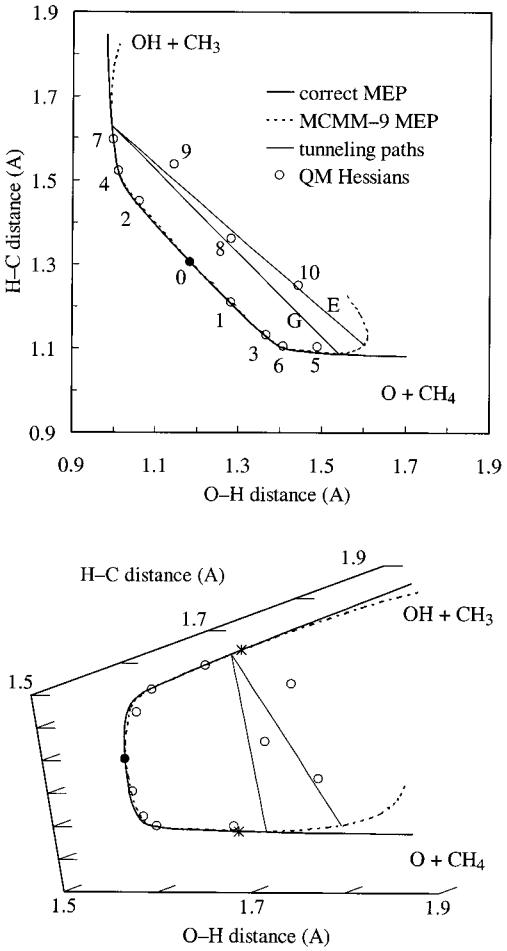

Figure 4. Same as Figure 2, except for the $O + CH_4 \rightarrow OH + CH_3$ reaction, and $-2.0\ a_0 < s < +2.0\ a_0$.

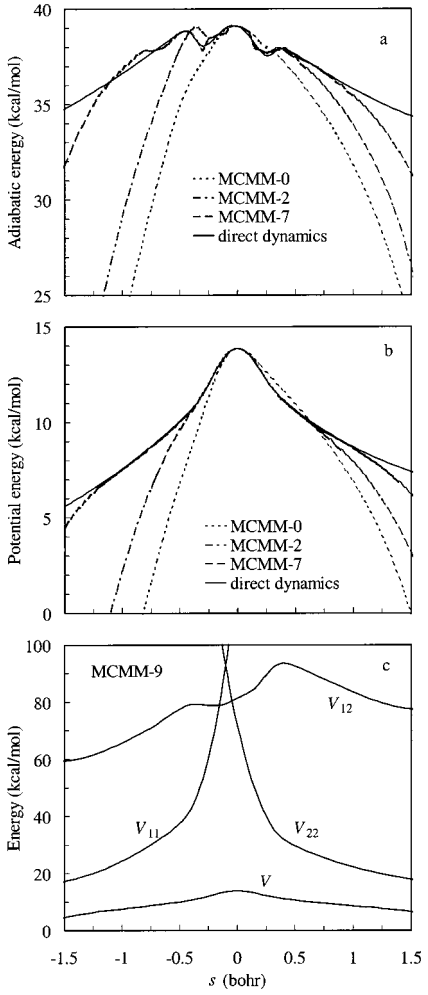

Figure 5. Same as Figure 3, except for the $O + CH_4 \rightarrow OH + CH_3$ reaction.

and the exit channels of the PES in isoinertial coordinates.[3,114,126] For the type of reaction given in eq 12, the skew angle is calculated as[114]

$$\beta = \cos^{-1}\sqrt{\frac{m_{CA}m_{BD}}{m_{CAH}m_{HBD}}} \qquad (14)$$

Figures 3, 5, 7, 9, 11, and 16 present, for all reactions, the matrix elements of the electronically diabatic Hamiltonian **V** along the MEP obtained in the MCMM−9 calculation, the potential energy $V_{MEP}(s)$, and the vibrationally adiabatic ground-state energy $V_a^G(s)$ obtained from MCMM calculations with various numbers of Shepard points and from the higher-level calculations. Figures 12, 13, and 14 show a series of contour plots for the $CH_2F + CH_3Cl$ system.

We investigated the rate constants over a wide range of temperatures. For each reaction, we selected two temperatures to present the comparison between the MCMM rate constants and the higher-level direct dynamics calculations. For five of the reactions (R-1 through R-5) the lower temperature is the one where tunneling is about 1 order of magnitude faster than overbarrier processes. These temperatures should provide a good test of how well the MCMM algorithm predicts the barrier width and the reaction-path curvature. The other temperature is chosen 100 K higher than the first one. For the other reaction (R-6) tunneling contributions are less important, and we take the two temperatures as 200 and 300 K because low temperatures provide stringent tests of theory.

The direct dynamics rate constants are in Table 3. The unsigned percentage deviation of the MCMM rate constants from the higher-level results averaged over the two temperatures shown for each reaction in Table 3 are given in Table 4 through 9 for the test cases investigated here. Tables 10 and 11 shows the errors obtained with the MCMM algorithm using the standard sequence of Shepard point placement averaged over all six reactions. To illustrate whether tunneling contributions into the vibrationally excited states are important, we give both LCT(0) and LCT results. Tables 4-11 do not show the errors in the CVT/LCT rate constants for the MCMM calculations (up to MCMM−7) where electronic structure information is available only along the MEP is available because these rate constants are typically overestimated by few order of magnitudes compared to the higher-level results. The reason is that the interpolation algorithm underestimates the potential energy surface in the concave region of the reaction path resulting in an unphysically big calculated tunneling coefficient, and we overcome this problem by adding points in this region.

The accuracy of the MCMM rate constants was monitored by means of two statistical measures of the average deviation.[114] We used the mean unsigned percentage error (MUPE), defined as

$$\mathrm{MUPE} = \left(\frac{1}{N}\sum_{i=1}^{N}\left|\frac{k_i^{MCMM} - k_i^{DD}}{k_i^{DD}}\right|\right) \times 100\% \qquad (15)$$

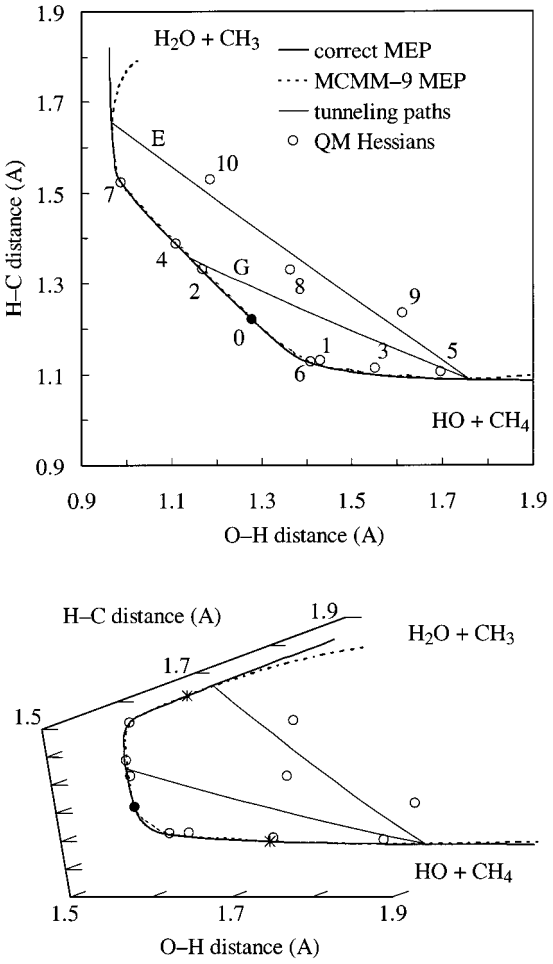

Figure 6. Same as Figure 2, except for the OH + $CH_4 \rightarrow H_2O + CH_3$ reaction, and $-2.5\ a_0 < s < +2.0\ a_0$.

and the logarithmically averaged percentage error (LAPE), defined by

$$\mathrm{LAPE} = (10^{\mathrm{AUPD}} - 1) \times 100\% \tag{16}$$

$$\mathrm{AUPD} = \frac{1}{N}\sum_{i=1}^{N}\left|\log_{10}\frac{k_i^{\mathrm{MCMM}}}{k_i^{\mathrm{DD}}}\right| \tag{17}$$

where k_i^{MCMM} represent the MCMM rate constants, k_i^{DD} are the direct dynamics results that the MCMM algorithm tries to reproduce, and N is the number of rate constants for which the comparison is made. Although it is very familiar and it is used more extensively, MUPE does not give an even-handed representation of the cases in which the rate constants are underestimated (those cases are limited to a percentage error of 100%), so we used LAPE in order to treat equivalently both underestimates and overestimates of the accurate rate constants. We use MUPE in Tables 4−10 and LAPE in Table 11. In discussing the results, we shall be very pleased whenever the error is less than 25% because the errors in the electronic structure data themselves almost always lead to errors at least this large. If we reduce the interpolation error below 25% it is almost surely not the dominant error. (In fact, experiments are seldom reliable to much better than 25%.)

Additional data (the actual MCMM rate constants, the Shepard point energies and geometries, and the internal coordinates used in the vibrational analysis of the normal modes along the MEP) are provided as Supporting Information.

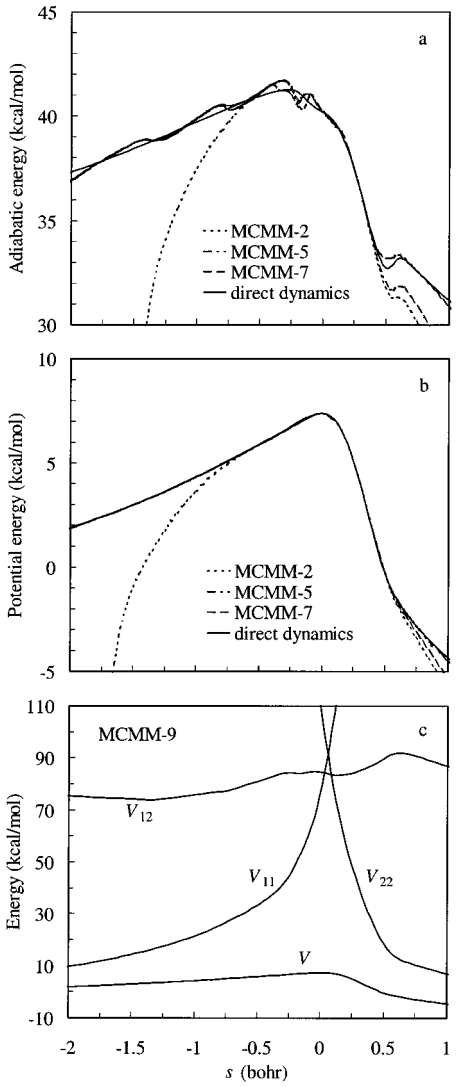

Figure 7. Same as Figure 3, except for the OH + $CH_4 \rightarrow H_2O + CH_3$ reaction.

8. Discussion

8.1. Cl + HBr → HCl + Br. For this reaction, we use MP2-(FC)/6−31G(d) method[33] for the electronic structure calculations. We choose this level of theory because the calculated classical barrier height for the forward reaction, 11.89 kcal/mol, is high enough for the tunneling to be very significant and therefore to provide a good test of MCMM. At the level of theory used here, the system is bent at the saddle point and along the reaction coordinate; the Cl−H−Br angle is 148 degrees at the saddle point, 110 degrees at $-1.50\ a_0$, and 118 degrees at $+1.50\ a_0$ in the direct dynamics calculation.

Two-dimensional representations of the reaction paths determined in the MCMM−9 run and in the direct dynamics calculation are plotted in Figure 2. The axes are the distances of the making and the breaking bonds, Cl−H and H−Br, respectively. In the lower panel of Figure 2, the axes make an angle of 12 degrees, which is the skew angle. The variational transition state is located on the reactant side of MEP, so the $\alpha = 1$, 3, 5, and 6 points are chosen on the reactant side, which is the high side for this reaction, and the $\alpha = 2$, 4, and 7 points are chosen on the product side, which is the low side. The $\alpha = 8$, 9, and 10 points are located in the concave side of the reaction path. The location of all points was determined following the

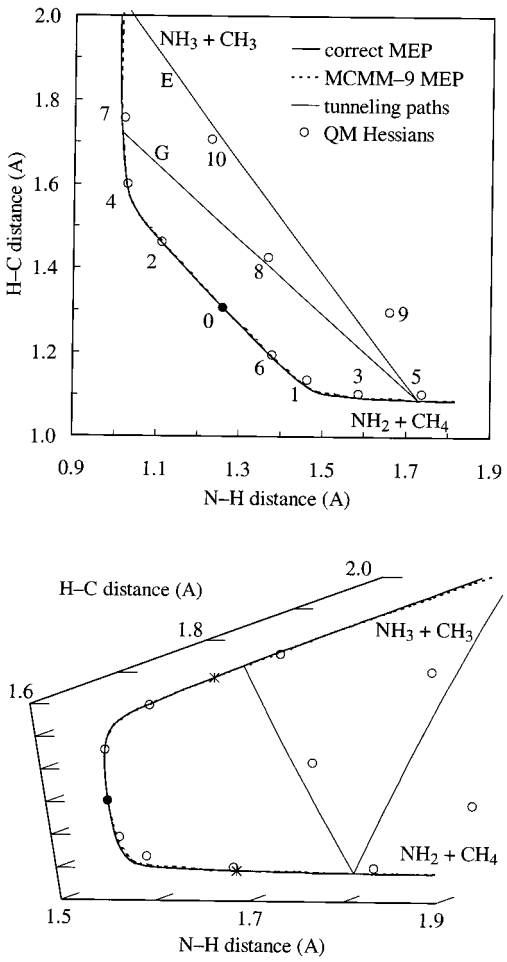

Figure 8. Same as Figure 2, except for the $NH_2 + CH_4 \rightarrow NH_3 + CH_3$ reaction, and $-2.0\ a_0 < s < +2.4\ a_0$.

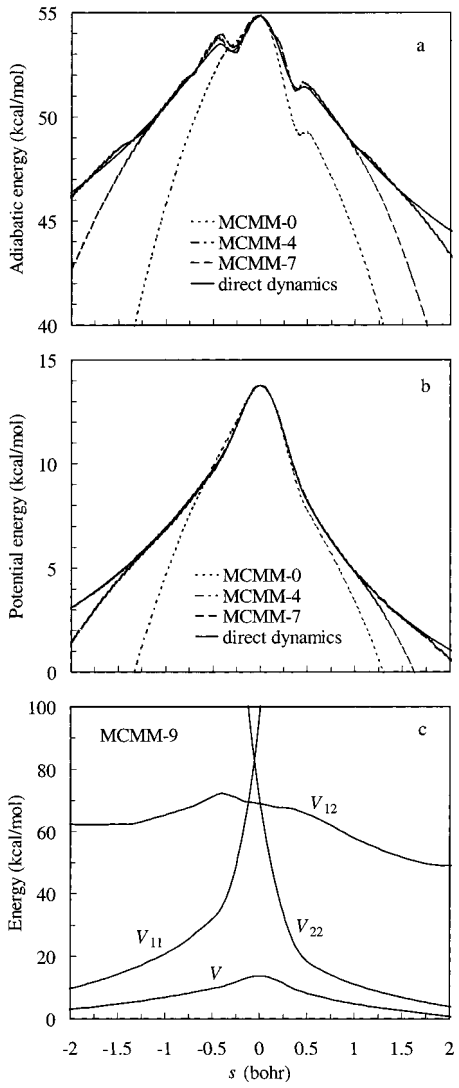

Figure 9. Same as Figure 3, except for the $NH_2 + CH_4 \rightarrow NH_3 + CH_3$ reaction.

standard sequence presented above. Accordingly, the $\alpha = 9$ point is closer to the high side (reactant side in this case) and $\alpha = 10$ point is closer the low side (product side). Two-dimensional representations of the tunneling paths into the ground state and into first vibrationally excited state for the energy equal to $0.50V_a^{HG} + 0.50V_a^{\ddagger G}$ are also presented in Figure 2. These tunneling paths appear curved in Figure 2 because the actual tunneling path is a straight line in isoinertial coordinates[19,50] and not in the coordinate system used for this representation.

The potential energy and the vibrationally adiabatic ground-state energy along the MEP from three MCMM calculations and the accurate calculation are shown in Figure 3b and 3a, respectively. The MCMM$-\alpha$ method for $\alpha \geq 7$ gives good agreement with direct dynamics for both the $V_{MEP}(s)$ and $V_a^G(s)$ curves over a wide s range. When the $\alpha = 8$, 9, and 10 points are included in the calculation, these curves do not change significantly because the Shepard points are in the concave side of the reaction path and significantly removed from the MEP. The diabatic potential matrix elements and the lowest electronically adiabatic potential energy surface along the MCMM$-$9 reaction path are plotted in Figure 3c. The resonance integral function V_{12} takes large values at $s < -1.5\ a_0$, but this has a negligible effect on the lowest eigenvalue because of the very big difference between $|V_{11} - V|$ and $|V_{22} - V|$.

This reaction has small variational effects. Tunneling is very significant, and E_{rep} is 2.65 and 0.95 kcal/mol below V_a^{AG} at 300 and 400 K, respectively. The MCMM method reproduces the accurate rate constants at all dynamical levels with a small number of ab initio Hessians (Table 4). The CVT/SCT rate constants are reasonably well converged with as little as one nonstationary Hessian. For this reaction, we were especially interested in investigating the tunneling into excited states and determining whether the MCMM algorithm can reproduce this. It was shown, using an analytical potential energy surface, that the collinear reaction between Cl and HBr is dominated by large-curvature tunneling into excited states.[46] This is not the case here where SCT dominates LCT. We found however that the direct dynamics CVT/LCT rate constant increases from 1.45×10^{-17} to 1.61×10^{-17} cm^3 molecule^{-1} s^{-1} at 300 K when tunneling into excited states is considered. The MCMM$-$9 calculations reproduce this well with the corresponding calculated rate constants being 1.40×10^{-17} and 1.54×10^{-17} cm^3 molecule^{-1} s^{-1}.

8.2. $O + CH_4 \rightarrow OH + CH_3$. The hydrogen-abstraction reaction from CH_4 by $O(^3P)$ is an important process in methane combustion and has been investigated both experimentally and theoretically.[30,127−133] These studies show that tunneling is significant at low temperature, and therefore this reaction is a good test case for our interpolation method. This reaction presents some computational challenges because the approach of the O atom along the H$-$C bond has a 3-fold symmetry that leads to a Jahn$-$Teller[134] effect. The potential energy does not

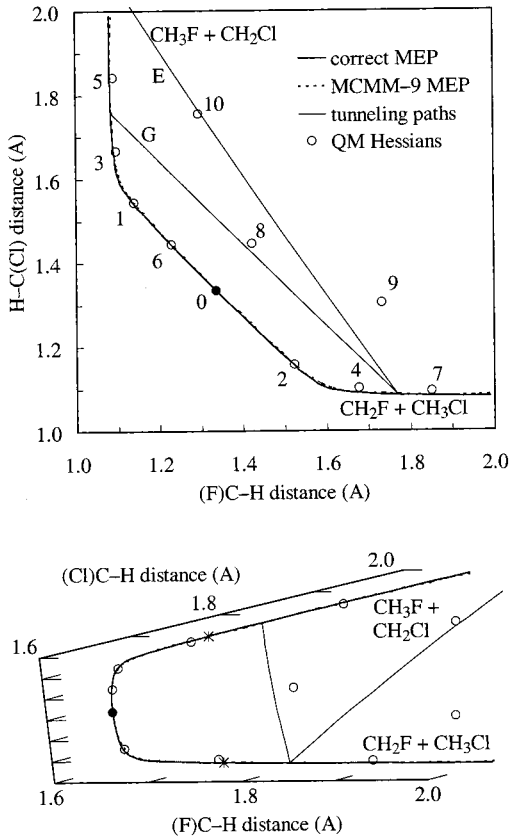

Figure 10. Same as Figure 2, except for the $CH_2F + CH_3Cl \rightarrow CH_3F + CH_2Cl$ reaction, and $-2.5\ a_0 < s < +2.4\ a_0$.

have a saddle point on the axis of symmetry but rather three with the O displaced off the axis. This lowers the symmetry of the saddle points to C_s, and splits the ^3E state into two electronic states of symmetry $^3A'$ and $^3A''$.[30,133,135] These surfaces are similar, with $^3A''$ being the lowest at the MPW1K/6−31+G-(d,p) level of theory[43] used here. We assumed that the dynamics are similar on both surfaces, and we therefore calculate the rate constant for the whole reaction as twice the rate constant for the lowest PES. The reaction is endothermic with a zero-point-exclusive endoergicity of 7.81 kcal/mol and an intrinsic barrier height of 6.04 kcal/mol (Table 1). Accordingly, the high side is the product side ($V_a^{HG} = V_a^{PG}$), and the low side is the reactant side ($V_a^{LG} = V_a^{RG}$).

The MCMM−0 calculation uses information (geometries, energies, gradients, and Hessians) at only three points: the O···CH_4 van der Waals molecule determined using molecular mechanics, the OH···CH_3 van der Waals molecule determined using molecular mechanics, and the saddle point ($\alpha = 0$) determined using electronic structure theory. The dynamical bottleneck is located in the reactant valley in the MCMM−0 calculation and in all the other MCMM calculations as well. Accordingly, the supplementary Shepard points $\alpha = 1$, 3, 5, and 6 are chosen on the reactant side (negative s) and the $\alpha = 2$, 4, and 7 points are chosen on the product side (positive s) of the MEP. Figure 4 shows two-dimensional representations of the locations of the Shepard points calculated using electronic structure theory as well as the MEP determined by direct dynamics and in the MCMM−9 calculations. We choose the axes to be the internal coordinates of the making and breaking bonds, O−H and H−C, respectively. Notice that the points in the MCMM data set do not all have the same values of the coordinates (for example, H−C−H bond angles) that are not shown, nor do they have optimized values for those coordinates.

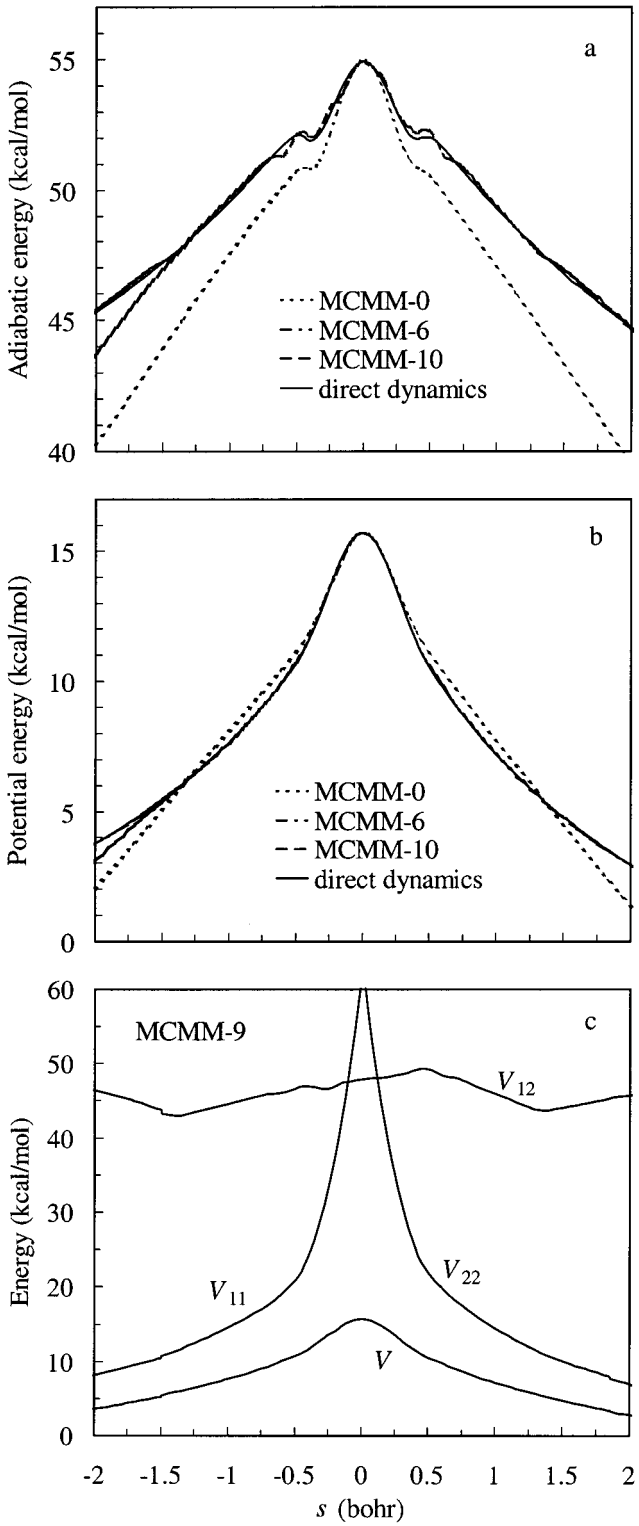

Figure 11. Same as Figure 3, except for the $CH_2F + CH_3Cl \rightarrow CH_3F + CH_2Cl$ reaction.

The two distances used as axes in Figure 4 as well as the distance between the other atoms involved in the bond breaking and making, O−C, are used in calculating the generalized distance according to eqs 11 and 13. It should be pointed out that, because the O−H−C angle is about 180 degrees along reaction coordinate (for example, 179 degrees at the saddle point, 177 degrees at $-1.50\ a_0$, and 179 degrees at $+1.50\ a_0$ in the direct dynamics calculation), the O−C distance is well approximated as the sum of O−H and H−C for this reaction.

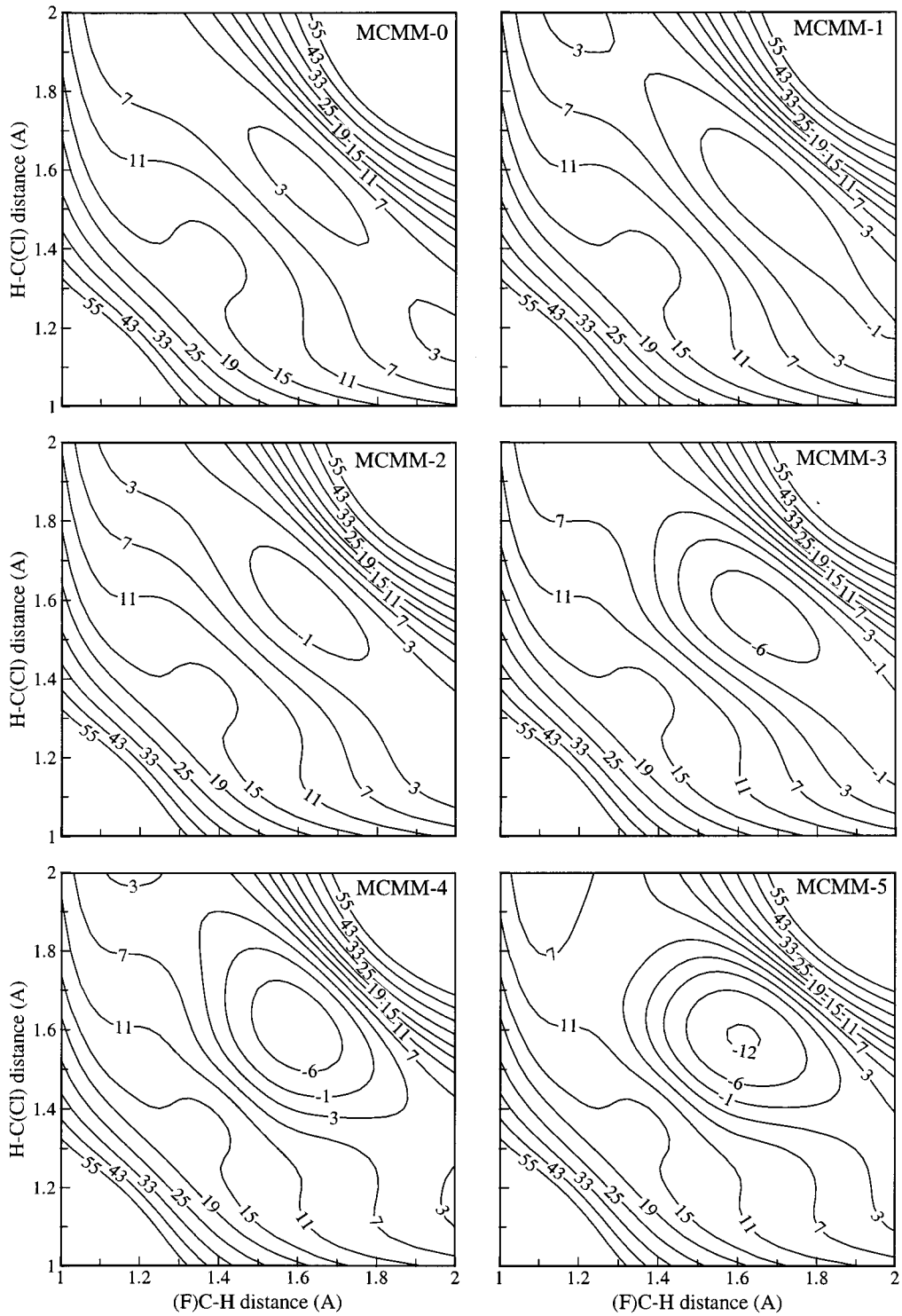

Figure 12. Equipotential contours for the $CH_2F + CH_3Cl \rightarrow CH_3F + CH_2Cl$ reaction obtained in MCMM−0 through MCMM−5 calculations.

Supplementary Shepard points $\alpha = 8$, 9, and 10 are located in the reaction swath region on the concave side of the reaction path. The representation of the MEP obtained in the MCMM−9 run shows good agreement with the accurate MEP (Figure 4) in the region where electronic structure Hessians are available, and deviations in the regions where it is extrapolated. Because of the potential energy underestimation in the corner-cutting region, the MCMM-determined MEP has a tendency to turn toward inside. The deviations are bigger on the reactant side, but one should have in mind that the $\alpha = 10$ point, which is supposed to improve the PES in that region, is not contained in the MCMM−9 calculation and the results (not shown) are improved once that point is included. It should be pointed out that the *s* range represented in Figure 4 is actually wider than that of the one required for the dynamics calculations.

The potential energy along the reaction coordinate for the direct dynamics calculation and three MCMM calculations are represented in Figure 5b, and the vibrationally adiabatic ground-state potential energies are graphed in Figure 5a. We choose three MCMM calculations that are most representative to illustrate the changes in $V_{MEP}(s)$ and $V_a^G(s)$. Both the $V_{MEP}(s)$ and the $V_a^G(s)$ are too narrow in the MCMM−0 calculation, and they became closer to the direct dynamics curves as the

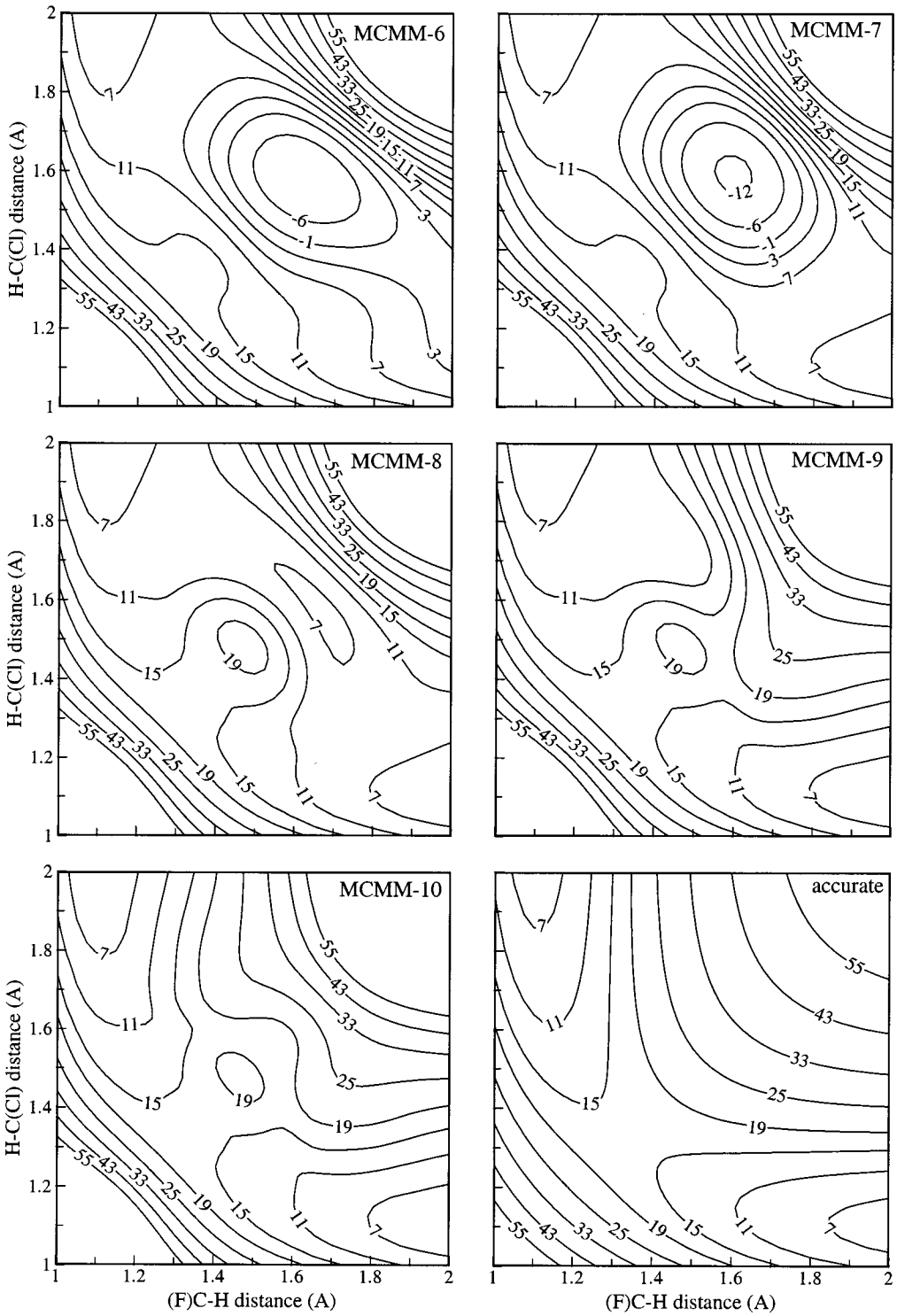

Figure 13. Equipotential contours for the $CH_2F + CH_3Cl \rightarrow CH_3F + CH_2Cl$ reaction obtained in MCMM−6 through MCMM−10 calculations and in the MPW1K/6−31+G(d,p) calculation.

number of Shepard points is increased. The MCMM−7 results are actually very similar to the accurate results between $s = -1.2\ a_0$ and $+1.0\ a_0$ along the reaction coordinate. The MCMM−8 through MCMM−10 curves are similar to the MCMM−7 ones because the $\alpha = 8$, 9, and 10 points are not located along the MEP and they have only a small influence on the shape of the potential along the MEP. In the direct dynamics calculation, the $V_{MEP}(s)$ curve (Figure 5b) reaches energies on the product side lower than the product energy of 7.81 kcal/mol, and the reason for this behavior is a strong complex formed between OH and CH_3, with an interaction energy of 2.36 kcal/mol. Interesting characteristics of the $V_a^G(s)$ curve and the low-temperature generalized free energy of activation profiles are the two local minima that appear one in the reactant valley and one in the product valley, which have also been seen in previous work.[30,136] These minima are correlated with local maxima in the curvature of the reaction path (these maxima are very clear in Figure 4) and are well reproduced by the MCMM calculations with six or more supplementary points. The elements of the matrix **V** and its

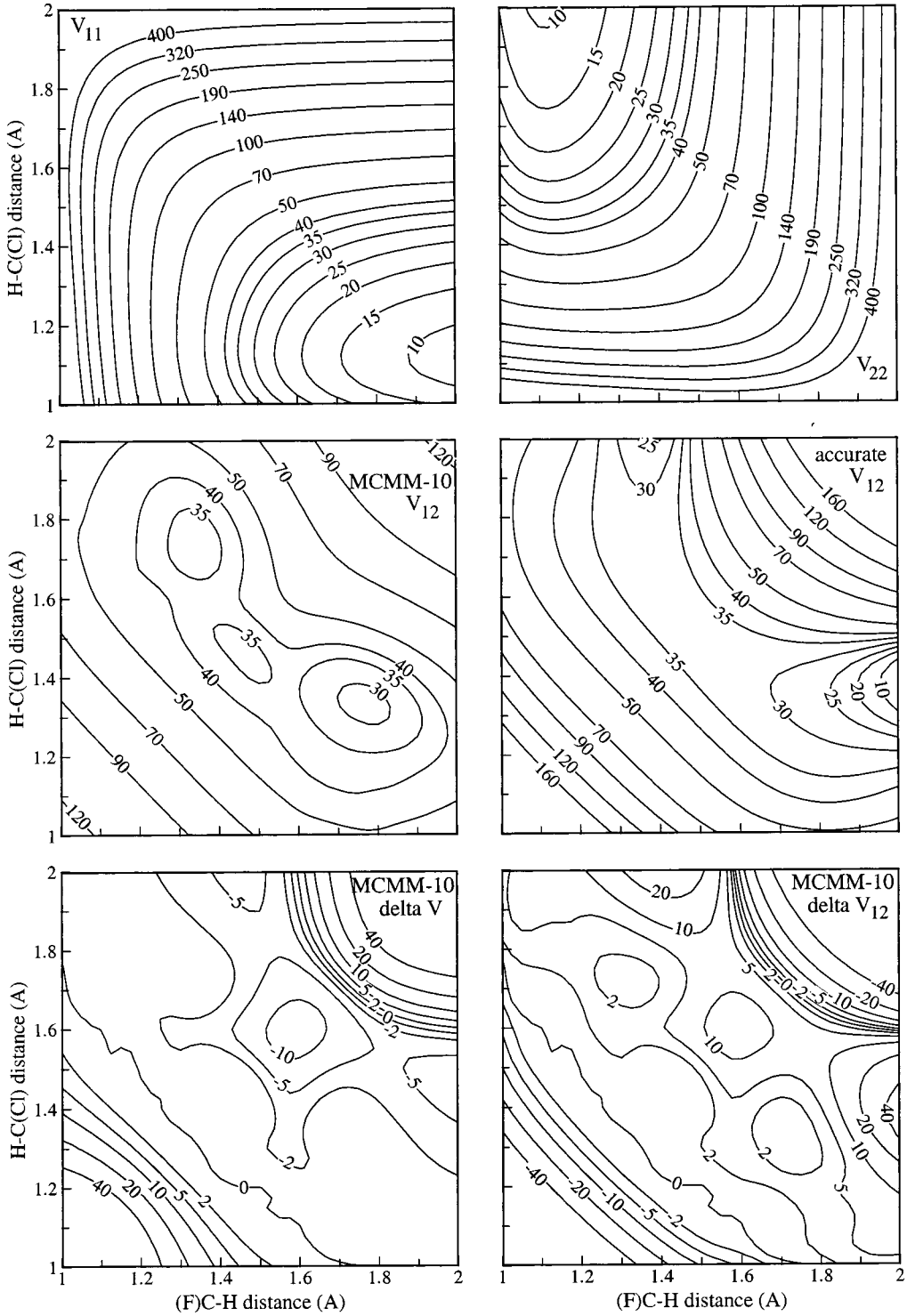

Figure 14. Molecular mechanics equipotential contours for the reactant and product configurations (V_{11} and V_{22}), the resonance integral equipotential contours for the MCMM−10 and the accurate PES (V_{12}), and the differences in the potential energy and in the resonance integral between the MCMM−10 and the MPW1K/6−31-G(d,p) surfaces.

lowest eigenvalue obtained in the MCMM−9 calculation are plotted in Figure 5c.

At the MPW1K/6−31+G(d,p) level of theory used here, the reaction is dominated by large-curvature tunneling, and E_{rep} is 3.39 and 1.18 kcal/mol below V_a^{AG} at 300 and 400 K, respectively. The direct dynamics calculation at the higher level give large transmission coefficients, 11.1 and 3.7 at these two temperatures. Table 5 gives the unsigned percentage errors of the MCMM rate constants from the higher-level results averaged over the two temperatures. Notice that the LCT calculation already become reasonable with the addition of the $\alpha = 8$ point, which is located at the middle of the path connecting the point on the low side (chosen on a 0.01 a_0 grid) at $V_a^G(s)$ of 33.97 kcal/mol (halfway between $V_a^{\ddagger G} = 39.10$ kcal/mol and $V_a^{LG} = 28.85$ kcal/mol) with the point on the high side (chosen again on a 0.01 a_0 grid) at $V_a^G(s)$ of 35.82 kcal/mol (halfway between $V_a^{\ddagger G} = 39.10$ kcal/mol and $V_a^{HG} = 32.55$ kcal/mol). In the MCMM−7 calculation, the potential energy at the $\alpha = 8$ point is 4.84 kcal/mol which is determined from elements of the **V**

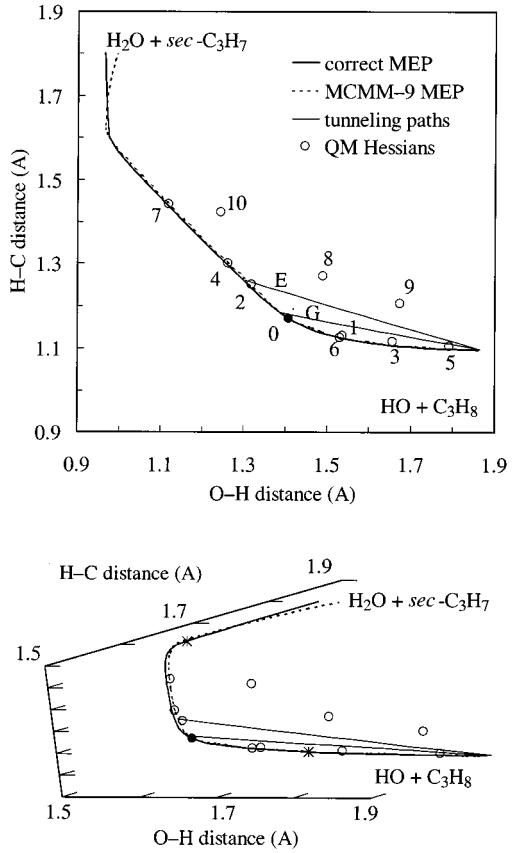

Figure 15. Same as Figure 2 except for the OH + $C_3H_8 \rightarrow H_2O$ + *sec*−C_3H_7 reaction, and $-2.5\ a_0 < s < +2.0\ a_0$.

matrix with the values $V_{11} = 78.94$ kcal/mol, $V_{22} = 65.86$ kcal/mol, $V_{12} = 67.24$ kcal/mol. In the MCMM−8 calculation, V_{12} becomes equal to 56.02 kcal/mol in order to reproduce the higher-level energy of $V = 16.00$ kcal/mol, with V_{11} and V_{22} being same as before. The deviations of the PES obtained with MCMM algorithm form the higher-level PES are bigger at points further from the MEP (e.g., at points along tunneling paths with termini at lower $V_a^G(s)$). The addition of one more point in the large-curvature region, $\alpha = 9$, brings the MCMM rate constants extremely close to the accurate results. For MCMM−9, an error of only 8% is obtained when averaging over the two temperatures investigated. The $\alpha = 10$ point does not improve the results significantly for this reaction. It is interesting to note that, if only CVT/SCT rate constants are desired, good accuracy in CVT/SCT rate constants is obtained with only five supplementary points along the MEP, in the MCMM−5 run. In this case, however, the CVT/SCT rate constants (Table 3) are more than three times smaller that those determined based on μOMT at 300 K and about half at 400 K, and this makes SCT be a poor approximation to μOMT.

The MCMM strategy we designed involves adding points in the regions necessary for obtaining accurate termini of large-curvature tunneling paths before the addition of the points in the LCT region. The classical turning points of the reaction-coordinate motion on the MEP determine these termini, and consequently, it is important to have a good description of the MEP over a wide *s* range. This is achieved by addition of the $\alpha = 5$ and 7 points. We also tested the possibility of adding supplementary Shepard points on the concave side of reaction path before adding the $\alpha = 5$, 6, and 7 points along MEP. The MCMM results obtained that way are less reliable at low

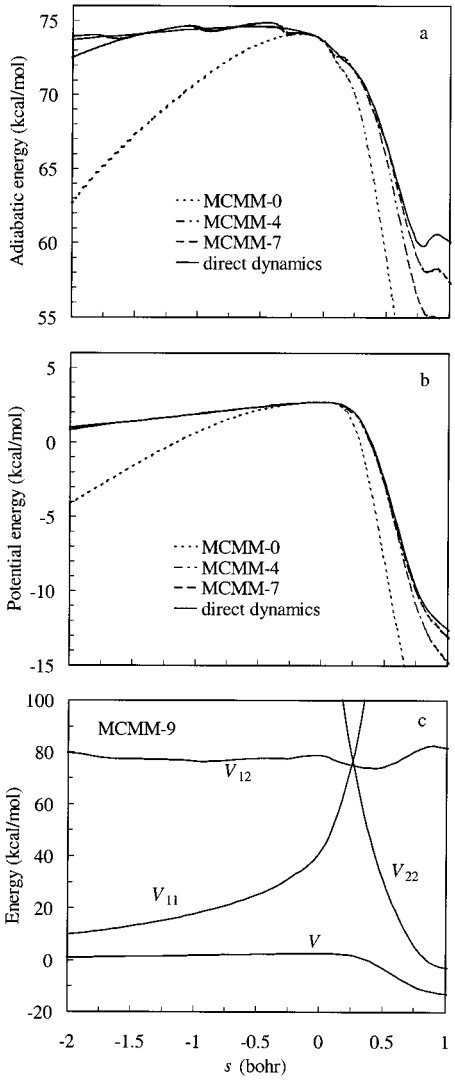

Figure 16. Same as Figure 3 except for the OH + $C_3H_8 \rightarrow H_2O$ + *sec*−C_3H_7 reaction.

temperature than are the results obtained using the standard sequence as presented above.

We[30] and others[136] had previously concluded, based on interpolation of MEP data through the LCT tunneling region or on an analytical PES of unknown validity in the LCT part of tunneling swath, that the LCT tunneling mechanism gave much larger rates than the SCT one does for this reaction, and the results presented in Table 3 confirm this, with the ratio of the LCT to the SCT result being a factor of 3.4 at 300 K. The results in Table 5 are very encouraging in that one can quantitatively reproduce the large LCT tunneling contributions with only two Hessians in the LCT portion of the reaction swath.

8.3. OH + $CH_4 \rightarrow H_2O + CH_3$. We employed MPW1K/6−31+G(d,p) method[43] for the electronic structure calculations for this reaction. At this level of theory, the calculated zero-point-exclusive exoergicity is 9.07 kcal/mol, and the intrinsic barrier height is 7.39 kcal/mol. Figure 6 presents two-dimensional representations of the reaction paths obtained in the MCMM−9 calculation and in the direct dynamics calculation, and the placement of the higher-level Shepard points. For this reaction, the skew angle determined in mass-scaled coordinates is 20 degrees so the entrance and exit valleys of the potential energy surface are graphed at this angle in the lower panel of Figure 6. This reaction presents a variational transition state on the reactant side of the saddle point in all MCMM

TABLE 3: Direct Dynamics Rate Constants (cm^3 $molecule^{-1}$ s^{-1}) for the Investigated Reactions at the Temperatures Where Comparison with the MCMM Results Is Made

T (K)	TST	CVT	CVT/ZCT	CVT/SCT	CVT/LCT(0)	CVT/LCT	CVT/μOMT
			$Cl + HBr \rightarrow HCl + Br$				
300	2.49(−18)[a]	2.09(−18)	6.92(−18)	3.03(−17)	1.45(−17)	1.61(−17)	3.05(−17)
400	1.70(−16)	1.40(−16)	2.20(−16)	5.05(−16)	2.90(−16)	3.31(−16)	5.10(−16)
			$O + CH_4 \rightarrow OH + CH_3$				
300	8.39(−19)	7.93(−19)	1.60(−18)	2.62(−18)	8.84(−18)	8.84(−18)	8.84(−18)
400	6.87(−17)	6.58(−17)	9.87(−17)	1.31(−16)	2.45(−16)	2.45(−16)	2.45(−16)
			$HO + CH_4 \rightarrow H_2O + CH_3$				
200	1.41(−17)	1.13(−18)	4.72(−18)	1.21(−17)	7.07(−18)	9.04(−18)	1.22(−17)
300	1.64(−15)	3.33(−16)	6.19(−16)	9.70(−16)	6.85(−16)	7.92(−16)	9.71(−16)
			$NH_2 + CH_4 \rightarrow NH_3 + CH_3$				
350	1.96(−20)	1.96(−20)	6.68(−20)	1.24(−19)	1.86(−19)	1.86(−19)	1.98(−19)
450	1.67(−18)	1.67(−18)	3.59(−18)	5.17(−18)	5.88(−18)	5.88(−18)	6.30(−18)
			$CH_2F + CH_3Cl \rightarrow CH_3F + CH_2Cl$				
350	2.49(−22)	2.49(−22)	1.30(−21)	2.47(−21)	3.04(−21)	3.04(−21)	3.39(−21)
450	3.53(−20)	3.52(−20)	9.87(−20)	1.45(−19)	1.41(−19)	1.41(−19)	1.59(−19)
			$HO + C_3H_8 \rightarrow H_2O + sec\text{-}C_3H_7$				
200	5.83(−14)	6.51(−15)	7.66(−15)	7.81(−15)	7.67(−15)	7.83(−15)	7.86(−15)
300	2.37(−13)	6.10(−14)	6.26(−14)	6.31(−14)	6.27(−14)	6.33(−14)	6.34(−14)

[a] $2.49(-18) \equiv 2.49 \times 10^{-18}$

TABLE 4: Mean Unsigned Percentage Error Averaged over Two Temperatures (300 and 400 K) for the Hydrogen-transfer Reaction $Cl + HBr \rightarrow HCl + Br$

method	CVT	CVT/ZCT	CVT/SCT	CVT/LCT(0)	CVT/LCT	CVT/μOMT
IVTST−0	20	840				
MCMM−0	11	85	110			
MCMM−1	11	10	25			
MCMM−2	11	18	19			
MCMM−3	11	11	10			
MCMM−4	11	10	10			
MCMM−5	11	11	11			
MCMM−6	5	5	15			
MCMM−7	4	5	15			
MCMM−8	4	5	15	5	4	15
MCMM−9	4	5	15	5	4	16
MCMM−10	4	5	15	5	4	16

TABLE 5: Mean Unsigned Percentage Error Averaged over Two Temperatures (300 and 400 K) for the Hydrogen-transfer Reaction $O + CH_4 \rightarrow OH + CH_3$

method	CVT	CVT/ZCT	CVT/SCT	CVT/LCT(0)	CVT/LCT	CVT/μOMT
IVTST−0	5	430				
MCMM−0	5	120	2000			
MCMM−1	5	14	570			
MCMM−2	5	10	140			
MCMM−3	3	7	61			
MCMM−4	3	6	43			
MCMM−5	2	3	2			
MCMM−6	5	2	4			
MCMM−7	5	1	1			
MCMM−8	5	1	1	27	27	28
MCMM−9	5	1	1	8	8	8
MCMM−10	5	0	1	8	8	8

TABLE 6: Mean Unsigned Percentage Error Averaged over Two Temperatures (200 and 300 K) for the Hydrogen-Transfer Reaction $HO + CH_4 \rightarrow H_2O + CH_3$

method	CVT	CVT/ZCT	CVT/SCT	CVT/LCT(0)	CVT/LCT	CVT/μOMT
IVTST−0	770	>5000				
MCMM−0	41	>5000	>5000			
MCMM−1	69	180	>5000			
MCMM−2	68	160	2400			
MCMM−3	67	40	27			
MCMM−4	66	39	29			
MCMM−5	66	42	34			
MCMM−6	45	15	19			
MCMM−7	46	16	22			
MCMM−8	46	18	24	18	37	25
MCMM−9	46	19	24	18	22	14
MCMM−10	46	19	23	18	8	15

TABLE 7: Mean Unsigned Percentage Error Averaged over Two Temperatures (350 and 450 K) for the Hydrogen-transfer Reaction $NH_2 + CH_4 \rightarrow NH_3 + CH_3$

method	CVT	CVT/ZCT	CVT/SCT	CVT/LCT(0)	CVT/LCT	CVT/μOMT
IVTST−0	0	350				
MCMM−0	7	48	490			
MCMM−1	7	3	37			
MCMM−2	7	15	4			
MCMM−3	7	13	9			
MCMM−4	7	13	10			
MCMM−5	7	13	9			
MCMM−6	7	18	16			
MCMM−7	7	18	16			
MCMM−8	7	19	16	200	200	190
MCMM−9	7	19	16	5	5	4
MCMM-10	7	19	16	8	8	6

calculations. Accordingly, the $\alpha = 1$, 3, 5, and 6 points are placed on the reactant side, and the $\alpha = 2$, 4, and 7 points are placed on the product side of the MEP. The $\alpha = 1$ and 2 points are added 1.85 kcal/mol ($^1/_4$ of IBH) below the saddle point, and the $\alpha = 3$ and 4 points are added 3.70 kcal/mol ($^1/_2$ of IBH) below the saddle point. The $\alpha = 5$ point is added 5.54 kcal/mol ($^3/_4$ of IBH) below the saddle point, the $\alpha = 6$ point is added 0.92 kcal/mol ($^1/_8$ of IBH) below the saddle point, and the $\alpha = 7$ point is added 8.94 kcal/mol ($^3/_4$ of $[V^{\ddagger} + (V^{\ddagger} - V^{P})]/2$) below the saddle point. The $\alpha = 8$ point is located at the middle of the path connecting the point on the high side at $V_a^G(s)$ of 37.30 kcal/mol (average of $V_a^{\ddagger G} = 40.19$ kcal/mol and $V_a^{HG} = 34.41$ kcal/mol) with the point on the low side at $V_a^G(s)$ of 32.12 kcal/mol (average of $V_a^{\ddagger G} = 40.19$ kcal/mol and $V_a^{LG} = 24.04$ kcal/mol). The $\alpha = 9$ and 10 points are located along the paths, determined in the MCMM−8 and MCMM−9 calculations, connecting the point on the high side at $V_a^G(s)$ of 35.86 kcal/mol ($^3/_4$ between $V_a^{\ddagger G}$ and V_a^{HG}) with the point on the low side at $V_a^G(s)$ of 28.08 kcal/mol ($^3/_4$ between $V_a^{\ddagger G}$ and V_a^{LG}),

TABLE 8: Mean Unsigned Percentage Error Averaged over Two Temperatures (350 and 450 K) for the Hydrogen-transfer Reaction $CH_2F + CH_3Cl \rightarrow CH_3F + CH_2Cl$

method	CVT	CVT/ ZCT	CVT/ SCT	CVT/ LCT(0)	CVT/ LCT	CVT/ μOMT
IVTST−0	0	160				
MCMM−0	0	110	200			
MCMM−1	0	34	92			
MCMM−2	0	1	9			
MCMM−3	0	4	16			
MCMM−4	0	7	21			
MCMM−5	0	8	23			
MCMM−6	0	3	3			
MCMM−7	0	2	4			
MCMM−8	0	3	4	170	170	160
MCMM−9	0	3	5	12	12	15
MCMM−10	0	3	5	10	10	13

TABLE 9: Mean Unsigned Percentage Error Averaged over Two Temperatures (200 and 300 K) for the Hydrogen-transfer Reaction $HO + C_3H_8 \rightarrow H_2O + sec-C_3H_7$

method	CVT	CVT/ ZCT	CVT/ SCT	CVT/ LCT(0)	CVT/ LCT	CVT/ μOMT
IVTST−0	540	620				
MCMM−0	150	740	1000			
MCMM−1	52	14	25			
MCMM−2	52	16	29			
MCMM−3	52	37	35			
MCMM−4	52	37	34			
MCMM−5	52	38	36			
MCMM−6	28	10	8			
MCMM−7	28	10	8			
MCMM−8	28	11	9	11	10	9
MCMM−9	28	11	9	11	9	8
MCMM−10	28	11	9	11	11	9

TABLE 10: Mean Unsigned Percentage Error Calculated by Averaging over All Six Test-case Reactions and Both Temperatures

method	CVT	CVT/ ZCT	CVT/ SCT	CVT/ LCT(0)	CVT/ LCT	CVT/ μOMT
IVTST−0	220	2400				
MCMM−0	36	2400	>5000			
MCMM−1	24	42	1000			
MCMM−2	24	36	440			
MCMM−3	23	19	26			
MCMM−4	23	19	24			
MCMM−5	23	19	19			
MCMM−6	15	9	11			
MCMM−7	15	9	11			
MCMM−8	19	9	11	72	75	70
MCMM−9	15	9	12	10	10	11
MCMM−10	15	9	12	10	8	11

with the $\alpha = 9$ point closer to the high side (reactant side for this reaction) and $\alpha = 10$ point closer the low side (product side).

Inspection of Figure 6 shows that $\alpha = 1$ and 6 points are located very close to each other. This is a quirk of the standard scheme that should be explained in more detail. The energies along the reaction coordinate in the MCMM runs with small number of higher-level data are not very accurate especially when extrapolated over a wide range. The location of the $\alpha = 1$ point is determined as the point at the energy of 5.53 kcal/mol (lower than saddle point by 1.86 kcal/mol) in the MCMM−0 calculation. The electronic structure calculation at that location gives a different energy, 6.14 kcal/mol, which means that the point is, on the higher-level PES that we try to reproduce, closer in energy to the saddle point, only 1.25 kcal/mol lower (about 17% of IBH). The PES determined in the MCMM−5 run is more accurate than the one in MCMM−0 run so when the $\alpha = 6$ point is chosen at 0.92 kcal/mol lower energy than the saddle point, its location is actually close to the $\alpha = 1$ point. It was our concern that the MCMM results may become unphysical when two higher-level Hessians are close to each other. In fact though, we found that the results very good even when such an "accident" occurs. This speaks well for the robustness of the standard scheme recommended here.

TABLE 11: Logarithmically Averaged Percentage Error Calculated by Averaging over All Six Test-case Reactions and Both Temperatures

method	CVT	CVT/ ZCT	CVT/ SCT	CVT/ LCT(0)	CVT/ LCT	CVT/ μOMT
IVTST−0	100	630				
MCMM−0	28	290	1100			
MCMM−1	43	29	180			
MCMM−2	43	25	87			
MCMM−3	41	25	29			
MCMM−4	41	24	28			
MCMM−5	40	26	24			
MCMM−6	20	10	13			
MCMM−7	20	10	13			
MCMM−8	20	11	13	45	48	48
MCMM−9	20	11	14	11	10	12
MCMM−10	20	11	14	11	9	12

The potential energy and the vibrationally adiabatic ground-state energies along the reaction coordinate from calculations with various numbers of electronic structure Hessians and from the direct dynamics calculation are shown in Figure 7b and 7a, respectively. Figure 7c shows the electronically diabatic Hamiltonian elements and the electronically adiabatic energy along the MEP calculated with nine supplementary points determined using the standard sequence. The $V_{MEP}(s)$ curves agree well with the accurate curve when seven or more supplementary points are added (Figure 7b). The MCMM−5 and MCMM−7 effective barriers (Figure 7a) shows an oscillating pattern on the reactant side of the saddle point. This is due to fluctuations in the MCMM frequencies along the MEP, a pattern observed also in the previous MCMM study.[60] Because the goal of applying MCMM is obtaining accurate rate constants, the oscillations do not need to be completely eliminated. The oscillations in the $V_a^G(s)$ curve become smaller when the $\alpha = 6$ point is added along the reaction path, and this can be seen by inspection of the MCMM−5 and MCMM−7 curves on the reactant side in Figure 7a.

The direct dynamics results (Table 3) show that this reaction has significant variational effects, with ratio k^{TST}/k^{CVT} of 12.5 at 200 K and 4.9 at 300 K. The deviations of the MCMM rate constants from the accurate ones averaged over two temperatures are presented in Table 6. The MCMM runs reproduce most of the variational effects; the CVT rate constants are however underestimated and this correlate with the errors in the $V_a^G(s)$ curves (MCMM curves give higher maximum that the accurate $V_a^G(s)$ curve). When the $\alpha = 6$ point is included in the calculation, the accuracy of the CVT rate constants is improved. The CVT/ZCT and even the CVT/SCT rate constants are actually easier to calculate than CVT ones. The tunneling calculations involve integrals over s (which smooth out some kinds of interpolatory noise) whereas CVT is based on a single point. In general, we are more interested in the results involving tunneling, but we are pleased that the algorithm is usually stable enough to yield accurate results even for the CVT rates.

The large-curvature tunneling contributions into the ground state are reproduce well in the MCMM−8 run while the contributions due to the tunneling into vibrationally excited states are better described as we add supplementary points $\alpha =$ 9 and 10. Considering the results for this reaction and the ones for R-1, we can say that the MCMM algorithm with the Shepard point placement presented here can accurately reproduce large-curvature tunneling into both the ground and the vibrationally excited states.

We[53,54,58,137−140] and others[61,141] have studied the rate constant for the OH + CH_4 reaction on several previous occasions, but in only a subset of these cases[54,61] was the large-curvature tunneling compared to the small-curvature one. In the first paper to include LCT calculations,[54] at 300 K, the CVT/LCT rate constant was smaller than the SCT one by 63% for one potential energy surface but larger than the SCT rate constant by 72% for another. In both cases though, the potential energy in the LCT part of the swath was interpolated on the basis of data along the MEP so the results were of uncertain reliability. In the second application to compare LCT to SCT,[61] based on direct dynamics, the LCT results were 31% lower than the SCT ones at 300 K. The present paper's direct dynamics calculations (Table 3) show that, at 300 K, the CVT/LCT rate constant is 18% smaller than the SCT one. This result is different from ref 61 because it is based on a different level of electronic structure calculations in the LCT part of the swath. Furthermore, Table 6 show that with the MCMM algorithm one can actually converge the LCT calculations for a given electronic structure level within 22% (and the μOMT calculations within 14%) with only two Hessians in the LCT part of the reaction swath. Thus, in the future it should be easier to avoid long-standing uncertainties about the dominant tunneling mechanism. Note that the results in Table 6 and some later tables do not converge as the number of Hessians at nonstationary points is increased. This is because we are not increasing the grid density. If the goal of the present paper were to demonstrate convergence, then we would use a different scheme for adding points; for example, we would add points halfway between previous points.

8.4. NH_2 + CH_4 → NH_3 + CH_3. For this reaction, all MCMM calculations use the molecular mechanics $NH_2\cdots CH_4$ well, the molecular mechanics $NH_3\cdots CH_3$ well, and the saddle point ($\alpha = 0$) calculated with MPW1K/6−31+G(d,p) method.[43] We find that the dynamical bottleneck is located very close to the saddle point, on the reactant valley side, therefore the $\alpha =$ 1, 3, 5, and 6 points are chosen on the reactant side, and the α = 2, 4, and 7 points are chosen on the product side of the MEP. Two-dimensional representations of the Shepard point locations as well as the MEPs obtained by direct dynamics and by the MCMM−9 calculation are graphed in Figure 8 with the axes at 90° in the higher panel and at 20 degrees in the lower panel. The axes we used are the making bond and the breaking bond, N−H and H−C, respectively. The N−C distance is smaller that the sum of the two because the N−H−C angle is smaller than 180 degrees (171 degrees at saddle point, 158 degrees at +1.5 a_0, and 163 degrees at −1.5 a_0 in the higher-level calculation). These three internuclear distances were used also in calculating the generalized distance (eqs 11 and 13) for this reaction.

The potential energy and the vibrationally adiabatic ground-state energy along the MEP calculated at the higher-level and with various numbers of supplementary Shepard points are plotted in Figure 9a, b. Compared to the accurate results, the $V_{MEP}(s)$ and $V_a^G(s)$ curves are too narrow in the MCMM−0 calculation, whereas the MCMM−7 results are very similar to the direct dynamics curves for a wide range of s. The region of agreement includes the local maxima and minima of the $V_a^G(s)$ curve in the reactant valley and in the product valley. The MCMM−4 curves are similar to the higher-level curves close to the saddle point but less accurate over a wider range.

Figure 9c shows that the molecular mechanics potential V_{11} of the reactant configuration on the product side of the saddle point and the molecular mechanics potential V_{22} of the product configuration on the reactant side of the saddle point are extremely large. This is a result of using a Taylor series expansion of the reactant and product wells that include the making and breaking bonds. As in the previous application of the MCMM algorithm,[60] it was found that the method is more robust when the Taylor series are used compared to the case where the making and breaking bonds are represented by Morse curves. In particular, to obtain correct results with a real-valved V_{12} function, the smaller of V_{11} and V_{22} must be larger than the correct V.

This reaction is dominated by large-curvature tunneling at both temperatures (see Table 3). The representative tunneling energy is 3.30 and 1.35 kcal/mol lower than V_a^{AG} at 350 and 450 K, respectively. Table 7 gives the mean unsigned percentage errors averaged over these two temperatures for calculations with various numbers of supplementary Shepard points. The MCMM−0 rate constants overestimate the accurate results as a result of the narrow barrier obtained by interpolation. However, the CVT, CVT/ZCT, and CVT/SCT results all converge very well with only two supplementary Shepard points.

The CVT/LCT rate constants are overestimated before we add points in the LCT region of the reaction swath, and, as for the previously discussed reactions, this is the result of potential energy surface being underestimated in that region. It is interesting to analyze the energy at the point $\alpha = 8$ in the MCMM−7 and MCMM−8 calculations. This point is located halfway along the straight line in Cartesian coordinates connecting the point on the high side with $V_a^G(s) = 48.03$ kcal/mol (the average between the $V_a^{\ddagger G} = 54.82$ kcal/mol and the $V_a^{HG} =$ 41.25 kcal/mol) with a point on the low side with $V_a^G(s) =$ 47.17 kcal/mol (the average between the $V_a^{\ddagger G} = 54.82$ kcal/mol and the $V_a^{LG} = 39.52$ kcal/mol). In the MCMM−7 run, the electronically diabatic matrix elements are $V_{11} = 71.33$ kcal/mol, $V_{22} = 62.71$ kcal/mol, and $V_{12} = 62.94$ kcal/mol which results in $V = 3.93$ kcal/mol at the $\alpha = 8$ point. In the MCMM−8 calculation, however, V equal 18.57 kcal/mol which gives $V_{12} = 48.26$ kcal/mol. Comparing this value to those in Figure 9 we see that V_{12} must be smaller in the LCT portion of the reaction swath than on the MEP. This is physically reasonably, i.e., the resonance energy should be less if both bonds are broken concertedly.[88,96]

The CVT/LCT rate constants are well converged in the MCMM−9 run, that is, with the addition of only two points in the LCT region. The addition of the $\alpha = 10$ point does not significantly change the accuracy of the rate constants, indicating that the results are well converged.

8.5. CH_2F + CH_3Cl → CH_3F + CH_2Cl. The electronic structure calculations were carried out using MPW1K/6−31+G-(d,p) method.[43] The reaction is almost thermoneutral at this level of theory, the zero-point-exclusive reaction energy being −1.32 kcal/mol. The van der Waals wells describing the reactant and the product configuration, $CH_2F\cdots CH_3Cl$ and $CH_3F\cdots CH_2Cl$, respectively, are used in Shepard interpolation. This reaction has no significant variational effects, the dynamical bottleneck being located close to the saddle point, on the product side. Following the standard sequence of adding Shepard points, the $\alpha = 1$, 3, 5, and 6 points are chosen on the product side, and

the $\alpha = 2$, 4, and 7 points are located on the reactant side of the MEP. Figure 10 shows the two-dimensional locations of all the higher-level Hessian information used for this reaction, and the MEPs obtained by the direct dynamics and in the MCMM−9 calculation. In the lower panel, the entrance and exit channels (as well as the axes) make an angle of 13 degrees, which is the skew angle. The tunneling paths into the ground state and the first vibrationally excited state in the MCMM−9 calculation, with of energy of 47.69 kcal/mol (the average between the $V_a^{\ddagger G} = 54.92$ kcal/mol and the $V_a^{HG} = 40.47$ kcal/mol), are also represented. Although close to being linear, the plotted tunneling paths are again not actually straight lines in these representations.

Figure 11a,b shows the potential energy and the adiabatic ground-state energy obtained in the direct dynamics calculation and for three MCMM calculations, and Figure 11c shows the elements of the matrix **V** determined along the MEP in the MCMM−9 run. The $V_{MEP}(s)$ and $V_a^G(s)$ curves obtained in the MCMM−0 run show again a good agreement with accurate ones only over a narrow range near the saddle point. The curves obtained in calculations with more electronic structure data, MCMM−6 and MCMM−10, agree well over a wide range along the MEP. The MCMM−6 and MCMM−10 curves are actually extremely similar to each other, illustrating that the addition of higher-level Hessian information on the LCT region does not change the MEP significantly. (This would not be the case for other, less optimized schemes for adding data points.)

The direct dynamics rate constants are given in Table 3, and the deviations of the MCMM rate constants from these values averaged over two temperatures are given in Table 8. In this case, good accuracy for CVT/SCT rate constants is obtained with only one point on each side of the saddle point. This may be however a fortuitous cancellation of errors because addition of more electronic structure information actually increases slightly the error (MCMM−3 through MCMM−5). When the $\alpha = 6$ point is included in the calculation the CVT/SCT rate constants are actually very close to the ones obtained in the direct dynamics calculation. The CVT/LCT rate constants are overestimated by few order of magnitudes until we add points on the concave side of the reaction path. The results improved as we add more Shepard points in the LCT region. The MCMM−9 results overestimate the accurate rate constants by less than 15% when averaged over two temperatures (350 and 450 K). The rate constant accuracy improves just slightly as we add the $\alpha = 10$ point.

Another interesting observation is that the reaction is dominated by large-curvature tunneling at 350 K and by small-curvature tunneling at 450 K (Table 3). Gratifyingly, the MCMM−9 and MCMM−10 calculations show the same trend as the direct dynamics in that LCT dominates at the lower temperature and SCT dominates at the higher temperature, and they reproduce well the changes in the dominant tunneling mechanism with temperature. The MCMM method also reproduces the fact that the contribution of large-curvature tunneling into excited states is insignificant for this reaction.

We present in Figures 12 and 13 a series of contour plots of the potential energy surface *V* determined in the MCMM runs and of the accurate potential energy surface. The axes are, as in Figure 10, the internuclear distances of the (F)C−H making bond and the H−C(Cl) breaking bond. The other internal coordinates are set equal to their values at the saddle point, and in this respect, this graphical representation is different than the one in Figure 10. The MCMM surfaces become more accurate in the regions where the supplementary Shepard points are added. Similar to the cases discussed above (R-2 and R-4), the potential energy in the large-tunneling path region of the PES is underestimated before the addition of the $\alpha = 8$, 9, and 10 points. As those points are included in calculation, the MCMM−10 surface becomes similar to the accurate surface over a wider region that includes the dynamically interesting region.

For the same geometries as in Figures 12 and 13, Figure 14 gives the equipotential contours of the molecular mechanics potentials V_{11} and V_{22}, the resonance energy function V_{12} from the MCMM−10 and the accurate surfaces, and the differences in V_{12} and in *V* between the MCMM−10 and the accurate results. It is interesting to note that the differences between the MCMM−10 values and those for the accurate surfaces are, in absolute value, smaller for the potential energy surface *V* that for the resonance integral V_{12}.

8.6. OH + C_3H_8 → H_2O + *sec*−C_3H_7. This reaction is investigated using the MPW1K/6−31+G(d,p) level of theory. For the hydrogen abstraction reaction at the secondary site of propane by hydroxyl radical, this electronic structure method gives a very small barrier height of 2.96 kcal/mol (Table 1), and small tunneling contributions are expected even at small temperature. For this reaction, we choose to make the comparison with the accurate rate constants at two low temperatures 200 and 300 K where the tunneling coefficients do not exceed the value of 2 in the higher-level direct dynamics calculation. Although tunneling contributions are not significant, the reaction presents big variational effects with a k^{TST}/k^{CVT} ratio of 9.0 at 200 K in the direct dynamics calculation, and it was therefore interesting to include this reaction in our test suite. Reaction rates at low temperature are also very sensitive to the frequencies, again providing a challenging test. Furthermore, we wanted to demonstrate that the MCMM algorithm is applicable to larger systems (this reaction has 13 atoms).

Figure 15 shows two-dimensional representations of the Shepard point locations as well as the MEP obtained in the MCMM−9 calculation and in the direct dynamics calculation. For this system, the skew angle is 16 degrees. The making bond O−H and the breaking bond H−C are the axes, and these two distances plus the O−C distance were used also in calculating the generalized distance between points in Shepard interpolation scheme for this reaction. Similarly to reaction R-3, we found in this case that, following the standard sequence, the $\alpha = 6$ point is very close to the $\alpha = 1$ point as a result of the relative inaccuracy of the MCMM runs with small number of electronic structure Hessians. The interpolation scheme and the MCMM rate constants are not adversely affected by the nearness of those electronic structure Hessians.

Figure 16b give the potential energies along the reaction path for three MCMM calculations and for the direct dynamics calculation. The vibrationally adiabatic ground-state potential energies are plotted in Figure 16a. The potential energy is very flat on the reactant side of the MEP, and this feature is well reproduced by the MCMM calculations. The $V_a^G(s)$ curves obtained in the MCMM runs show oscillations similar to the ones obtained in the OH + CH_4 case, but the amplitudes are smaller. Figure 16c shows the electronically diabatic matrix elements and electronically adiabatic eigenvalue along the reaction path obtained in the MCMM−9 calculation.

Table 9 gives the deviations of the MCMM rate constants from the accurate ones averaged over the two temperatures where the comparison is made. Relatively accurate results for CVT/ZCT and CVT/SCT rate constants are obtained with as few as one supplementary Shepard point because the tunneling

effects are small. The variational effects are also reproduced well. The accuracy of rate constants is greatly increased once the $\alpha = 6$ point is included in the calculation. Accurate CVT/LCT and therefore CVT/μOMT rate constants are obtained with as low as eight supplementary Shepard points. Addition of the $\alpha = 9$ and 10 points do not further change significantly the results because the rate constants are already well converged in the MCMM−8 calculation for this case.

9. Summary and Concluding Remarks

Tables 10 and 11 present the errors obtained in the MCMM calculations with the various numbers of additional nonstationary higher-level Hessians averaged over all six test reactions. We also included in the first row of each of these tables as well as Tables 4 through 9 the errors obtained when k^{CVT} is approximated by k^{TST} and when $k^{CVT/ZCT}$ is approximated by $k^{IVTST-0}$ ($k^{IVTST-0}$ is the rate constant calculated using interpolated variational transition-state theory[52]). The TST, IVTST−0, and MCMM−0 estimate of the rate constants are obtained using only information at stationary points and may considered as zero-order approximations to the accurate rate constants. The MCMM−0 results are more accurate than the IVTST−0 results.

Inspection of the results in Tables 10 and 11 shows that relative accurate CVT/ZCT and CVT/SCT rate constants are obtained with as little as three supplementary Shepard points for all reactions. Very accurate results (errors less than 25% for all reactions) are obtained in the MCMM−6 runs for CVT/ZCT and CVT/SCT rate constants, and in the MCMM−9 runs for CVT/LCT and CVT/μOMT rate constants. The results are just slightly improved in the MCMM−10 calculations. We have shown therefore that the MCMM calculations reproduce well both variational and tunneling effects of the higher-level dynamics with less than 10 nonstationary Hessians, and in some cases with as few as only two of them. For the higher temperatures, one could obtain good accuracy for all reactions with less electronic structure Hessians, but the recommended point sequence is more robust over a wider range of temperatures.

The CVT/LCT rate constants become relatively accurate only after electronic structure Hessians are added on the concave side of the reaction path. The CVT/LCT results are overestimated (sometimes by a few order of magnitude) before the addition of these points. It is our belief that the CVT/LCT rate constants calculated with MCMM−0 through MCMM−7 are, in general, meaningless and therefore we choose not to include them here. It is not surprising that the MCMM algorithm may produce unphysical outcome in regions where electronic structure information is not included, but it is very encouraging how fast the results become useful as points are added in the dynamically relevant region.

The sequence proposed here is chosen to yield accurate rate constants for a range of reactions with as few electronic structure Hessians as possible. We cannot emphasize too strongly that other point placement sequences can be found that give better results for one or another specific reactions. Our goal, however, was to find a single simple point placement rule that is robust enough to give good results for several quite different reactions. It is also noteworthy that we proposed a sequence that is independent of temperature so it can be used successfully over a wide range of temperatures.

The standard sequence of Shepard point placement up to the $\alpha = 5$ point gives a good overall shape to the reaction path in its most critical region and to the potential and effective potential along the reaction path in that region. The $\alpha = 6$ point gives a better description of the reaction path near the dynamical bottleneck and the CVT/SCT rate constants are well converged at this level. The $\alpha = 7$ point is used to describe a wider region of the reaction path for the purpose of calculating the termini of the large-curvature tunneling paths. The $\alpha = 8$ and 9 points, located in the concave side of the reaction coordinate, improve and converge the CVT/LCT rate constants but have almost no effect on the CVT/SCT rate constants. The $\alpha = 10$ point is used for an improved description of the tunneling contributions into vibrationally excited states.

By knowing that a reaction is dominated by small-curvature tunneling, one can obtain very accurate results with only six electronic structure Hessians and the addition of the $\alpha = 7$, 8, 9, and 10 points is not necessary. The two-dimensional representations of the reaction paths and the corner-cutting tunneling paths into the ground state give insight into the dominant tunneling mechanism. For example, for the LCT-dominated reactions, the tunneling paths into the ground state bypass both points of maximum curvature, whereas for the SCT-dominated reactions (and for reaction R-6 where LCT(0) < SCT) the large-curvature tunneling paths bypass only one point of maximum curvature (the one on the high side). This is not true for the tunneling paths into the first excited state.

The development of efficient methods for fitting potential energy surfaces for chemically reactive species is a long-standing goal of theoretical chemistry. Most methods that have been used so far require a large amount of human judgment, which leads to two major disadvantages: (1) they are very time-consuming, and (2) there is a danger that pre-conceived notions of the fitter will have significant consequences for the resulting fit, for example, it may be a human decision whether to add a bend−stretch interaction term. With these problems in mind we have trial to develop a fitting procedure that does not require so much human judgment. The present MCMM procedure represents, we believe, a major step forward in this regard. First of all, it is based on quadratic expansions that automatically include all cross terms. Second, it is reasonably automatic. The major human choice concerns the placement of points. Therefore, a primary goal of the present study was to demonstrate that one can obtain good results without specifically tailoring the point placement to the individual system at hand. To show this, we applied a single point-placement scheme in an automatic way to six different reactions and showed that we could obtain good fits for all six cases with a single scheme. The method provides good approximations both for tunneling along the reaction path and for corner-cutting tunneling effects.

A second major advantage of the method presented here is efficiency. This efficiency comes about because the method takes advantage of the existence of molecular mechanics functions for reactants and products. This means that high-level electronic structure information is needed only in the transition state and tunneling swath regions where reactant and product molecular mechanics expansions break down.

We have developed a general and robust protocol for the placement of the higher-level Shepard points. We compared the MCMM rate constants for the six reactions of the test suite with the direct dynamics results at two temperatures where the tunneling effects are important. Very good accuracy ($\leq$ 25%) for all the test reactions is obtained with nine nonstationary Hessian calculations. The results for large-curvature tunneling are systematically improved by adding more electronic structure data in the reaction swath. We found an average error of 11% for the MCMM calculations of CVT/μOMT rate constants averaged over two temperature for all reactions with nine

supplementary Shepard points and no deviation greater than 25% in the individual rate constants that include ZCT, SCT, LCT(0), LCT, or μOMT tunneling effects even at the lower temperature. Similar overall accuracy is obtained with 10 supplementary Shepard points, and the large-curvature tunneling results are slightly improved.

The accurate modeling of the dynamics of large systems is very demanding due to the computational cost. The MCMM algorithm minimizes the electronic structure input necessary to construct an approximate energy surface that can be used for dynamics calculations. We believe that the MCMM algorithm in the form presented here, or in forms slightly modified for application to a particular system, will allow more widespread application of variational transition state theory with optimized multidimensional tunneling contributions to large systems with higher levels of electronic structure theory.

Further testing will be required to ascertain the usefulness of MCMM for other types of dynamical calculations or with a tradeoff of more energies and gradients vs less Hessians, but the accuracy obtained here is very encouraging for expecting that it would be useful in a broader context as well, although the point placement may need further study for other uses.

Acknowledgment. This work was supported in part by the U.S. Department of Energy, Office of Basic Energy Sciences.

Appendix

Force Field Parameters for OH + CH_4 and OH + C_3H_8. The force field parameters used for these reactions were same as described in the previous paper.[60]

New Force Field Parameters for O + CH_4. A new atom type was defined for atomic oxygen. The van der Waals parameters for this atom type were taken to be the same as those of atom type 6 (which corresponds to O in C−O−H, C−O−C, or O−O).

New Force Field Parameters for NH_2 + CH_4. We used MM3's atom type 23 (which is used for H in amines or imines) for the hydrogen atoms in NH_2 and NH_3, and we used atom type 8 (which is used for N in sp^3 hybridization) for the nitrogen in NH_3. A new atom type was defined for the nitrogen atoms of the NH_2 radical. The force field parameters for this atom type (van der Waals, N−H bond stretching, and H−N−H angle bending parameters) were taken to be the same as those for atom type 8.

New Force Field Parameters for CH_2F + CH_3Cl. The force field parameters used for this reaction were same as described in the previous paper[60] except for the van der Waals distance parameter between the C atom in the sp^2 radical and the transferred H atom. This parameter was changed back from the value of 3.00 A used in ref 60 to the original MM3 value of 3.56 A, which makes a less tight structure for the reactant and product wells. (In the present article, any parameter that exists in the original MM3 force field is used without change; only missing parameters need to be given values.)

New Force Field Parameters for Cl + HBr. Five new atom types were defined for this reaction: H bonded to Cl or Br, chlorine atom, bromine atom, chlorine in H−Cl, and bromine in H−Br. The van der Waals parameters for the H, Cl (both new atom types), and Br (both new atom types) were taken to be the same as those for atom type 5 (defined as H except on N, O, or S), atom type 12 (chloride), and atom type 13 (bromide), respectively. The stretching force constant and equilibrium bond distance for the stretches between the H atom and the halogen atoms (Cl and Br) were chosen to be 5.16 mdyn/A and 1.2746 A for the H−Cl bond, and 4.12 mdyn/A and 1.4145 A for the H−Br bond, respectively.[142]

Supporting Information Available: The MCMM rate constants at the temperatures of interest are given for all six reactions. The Shepard points energies and selected geometric data are provided. We also give the set of internal coordinates used in the vibrational analysis of the generalized normal modes along the MEP for all test cases. This material is available free of charge via the Internet at http://pubs.acs.org.

References and Notes

(1) Garrett, B. C.; Truhlar, D. G. *J. Chem. Phys.* **1984**, *81*, 309.
(2) Truhlar, D. G.; Garrett, B. C.; Hipes, P. G.; Kuppermann, A. *J. Chem. Phys.* **1984**, *81*, 3542.
(3) Truhlar, D. G.; Isaacson, A. D.; Garrett, B. C. In *Theory of Chemical Reaction Dynamics*; Baer, M., Ed.; CRC Press: Boca Raton, FL, 1985; Vol. 4; p 65.
(4) Kreevoy, M. M.; Truhlar, D. G. In *Investigation of Rates and Mechanisms of Reactions*; Bernasconi, C. F., Ed.; John Wiley & Sons: New York, 1986; Vol. 6; p 13.
(5) Tucker, S. C.; Truhlar, D. G. In *New Theoretical Concepts Understanding Organic Reactions*; J. Bertran, I. G. C., Ed.; Kluwer Academic Publishers: Dordrecht, 1989; Vol. 267; p 291.
(6) Truhlar, D. G.; Garrett, B. C.; Klippenstein, S. J. *J. Phys. Chem.* **1996**, *100*, 12 771.
(7) Warshel, A.; Karplus, M. *Chem. Phys. Lett.* **1975**, *32*, 11.
(8) Leforestier, C. *J. Chem. Phys.* **1978**, *68*, 4406.
(9) Truhlar, D. G.; Duff, J. W.; Blais, N. C.; Tully, J. C.; Garrett, B. C. *J. Chem. Phys.* **1982**, *77*, 764.
(10) Car, R.; Parrinello, M. *Phys. Rev. Lett.* **1985**, *55*, 2471.
(11) Baldridge, K. K.; Gordon, M. S.; Steckler, R.; Truhlar, D. G. *J. Phys. Chem.* **1989**, *93*, 5107.
(12) Truhlar, D. G.; Gordon, M. S. *Science* **1990**, *249*, 491.
(13) Galli, G.; Parrinello, M. *NATO ASI Ser., Ser. E* **1991**, *205*, 283.
(14) Gonzalez-Lafont, A.; Truong, T. N.; Truhlar, D. G. *J. Phys. Chem.* **1991**, *95*, 4618.
(15) Hartke, B.; Carter, E. A. *J. Chem. Phys.* **1992**, *97*, 6569.
(16) Lu, D.-h.; Truong, T. N.; Melissas, V. S.; Lynch, G. C.; Liu, Y.-P.; Garrett, B. C.; Steckler, R.; Isaacson, A. D.; Rai, S. N.; Hancock, G. C.; Lauderdale, J. G.; Joseph, T.; Truhlar, D. G. *Comput. Phys. Commun.* **1992**, *71*, 235.
(17) Liu, Y. P.; Lynch, G. C.; Truong, T. N.; Lu, D. H.; Truhlar, D. G.; Garrett, B. C. *J. Am. Chem. Soc.* **1993**, *115*, 2408.
(18) Liu, Y. P.; Lu, D. H.; Gonzalez-Lafont, A.; Truhlar, D. G.; Garrett, B. C. *J. Am. Chem. Soc.* **1993**, *115*, 7806.
(19) Truong, T. N.; Lu, D.-h.; Lynch, G. C.; Liu, Y.-P.; Melissas, V. S.; Stewart, J. J. P.; Steckler, R.; Garrett, B. C.; Isaacson, A. D.; Gonzalez-Lafont, A.; Rai, S. N.; Hancock, G. C.; Joseph, T.; Truhlar, D. G. *Comput. Phys. Commun.* **1993**, *75*, 143.
(20) Truhlar, D. G. In *The Reaction Path in Chemistry: Current Approaches and Perspectives*; Heidrich, D., Ed.; Kluwer: Dordrecht, 1995; Vol. 16; p 229.
(21) Cheng, H. P.; Barnett, R. N.; Landman, U. *Chem. Phys. Lett.* **1995**, *237*, 161.
(22) Jackels, C. F.; Gu, Z.; Truhlar, D. G. *J. Chem. Phys.* **1995**, *102*, 3188.
(23) Truong, T. N. *J. Chem. Phys.* **1995**, *102*, 5335.
(24) Gordon, M. S.; Chaban, G.; Taketsugu, T. *J. Phys. Chem.* **1996**, *100*, 11 512.
(25) Bueker, H.-H.; Helgaker, T.; Ruud, K.; Uggerud, E. *J. Phys. Chem.* **1996**, *100*, 15 388.
(26) Cheng, H.-P.; Krause, J. L. *J. Chem. Phys.* **1997**, *107*, 8461.
(27) Aida, M.; Yamataka, H.; Dupuis, M. *Chem. Phys. Lett.* **1998**, *292*, 474.
(28) Duncan, W. T.; Bell, R. L.; Truong, T. N. *J. Comput. Chem.* **1998**, *19*, 1039.
(29) Roberto-Neto, O.; Coitino, E. L.; Truhlar, D. G. *J. Phys. Chem. A* **1998**, *102*, 4568.
(30) Corchado, J. C.; Espinosa-Garcia, J.; Roberto-Neto, O.; Chuang, Y.-Y.; Truhlar, D. G. *J. Phys. Chem. A* **1998**, *102*, 4899.
(31) Bolton, K.; Bernhard Schlegel, H.; Hase, W. L.; Song, K. *Phys. Chem. Chem. Phys.* **1999**, *1*, 999.
(32) Truong, T. N.; Maity, D. K. *Comput. Chem.* (*Singapore, Singapore*) **2000**, *5*, 211.
(33) Pople, J. A.; Binkley, J. S.; Seeger, R. *Int. J. Quantum Chem., Symp.* **1976**, *10*, 1.
(34) Purvis, G. D.; III; Bartlett, R. J. *J. Chem. Phys.* **1982**, *76*, 1910.

(35) Raghavachari, K.; Trucks, G. W.; Pople, J. A.; Head-Gordon, M. *Chem. Phys. Lett.* **1989**, *157*, 479.
(36) Hirao, K. *Chem. Phys. Lett.* **1992**, *190*, 374.
(37) Raghavachari, K.; Anderson, J. B. *J. Phys. Chem.* **1996**, *100*, 12 960.
(38) *Chemical Applications of Density-Functional Theory*; Laird, B. B.; Ross, R. B.; Ziegler, T., Eds.; ACS Symposium series 629. American Chemical Society: Washington, DC, 1996.
(39) Curtiss, L. A.; Raghavachari, K.; Redfern, P. C.; Rassolov, V.; Pople, J. A. *J. Chem. Phys.* **1998**, *109*, 7764.
(40) Curtiss, L. A.; Raghavachari, K.; Redfern, P. C.; Pople, J. A. *J. Chem. Phys.* **2000**, *112*, 1125.
(41) Fast, P. L.; Sanchez, M. L.; Truhlar, D. G. *Chem. Phys. Lett.* **1999**, *306*, 407.
(42) Fast, P. L.; Corchado, J. C.; Sanchez, M. L.; Truhlar, D. G. *J. Phys. Chem. A* **1999**, *103*, 5129.
(43) Lynch, B. J.; Fast, P. L.; Harris, M.; Truhlar, D. G. *J. Phys. Chem. A* **2000**, *104*, 4811.
(44) Garrett, B. C.; Truhlar, D. G.; Wagner, A. F.; Dunning, T. H., Jr. *J. Chem. Phys.* **1983**, *78*, 4400.
(45) Bondi, D. K.; Connor, J. N. L.; Garrett, B. C.; Truhlar, D. G. *J. Chem. Phys.* **1983**, *78*, 5981.
(46) Garrett, B. C.; Abusalbi, N.; Kouri, D. J.; Truhlar, D. G. *J. Chem. Phys.* **1985**, *83*, 2252.
(47) Garrett, B. C.; Joseph, T.; Truong, T. N.; Truhlar, D. G. *Chem. Phys.* **1989**, *136*, 271.
(48) Kreevoy, M. M.; Ostovic, D.; Truhlar, D. G.; Garrett, B. C. *J. Phys. Chem.* **1986**, *90*, 3766.
(49) Truhlar, D. G.; Garrett, B. C. *Journal de Chimie Physique* **1987**, *84*, 365.
(50) Fernandez-Ramos, A.; Truhlar, D. G. *J. Chem. Phys.* **2001**, *114*, 1491.
(51) Truhlar, D. G.; Kilpatrick, N. J.; Garrett, B. C. *J. Chem. Phys.* **1983**, *78*, 2438.
(52) Gonzalez-Lafont, A.; Truong, T. N.; Truhlar, D. G. *J. Chem. Phys.* **1991**, *95*, 8875.
(53) Melissas, V. S.; Truhlar, D. G. *J. Chem. Phys.* **1993**, *99*, 1013.
(54) Hu, W. P.; Liu, Y. P.; Truhlar, D. G. *J. Chem. Soc., Faraday Trans.* **1994**, *90*, 1715.
(55) Ischtwan, J.; Collins, M. A. *J. Chem. Phys.* **1994**, *100*, 8080.
(56) Nguyen, K. A.; Rossi, I.; Truhlar, D. G. *J. Chem. Phys.* **1995**, *103*, 5522.
(57) Ishida, T.; Schatz, G. C. *J. Chem. Phys.* **1997**, *107*, 3558.
(58) Corchado, J. C.; Coitino, E. L.; Chuang, Y.-Y.; Fast, P. L.; Truhlar, D. G. *J. Phys. Chem. A* **1998**, *102*, 2424.
(59) Hollebeek, T.; Ho, T.-S.; Rabitz, H. *Annu. Rev. Phys. Chem.* **1999**, *50*, 537.
(60) Kim, Y.; Corchado, J. C.; Villa, J.; Xing, J.; Truhlar, D. G. *J. Chem. Phys.* **2000**, *112*, 2718.
(61) Huang, C.-H.; You, R.-M.; Lian, P.-Y.; Hu, W.-P. *J. Phys. Chem. A* **2000**, *104*, 7200.
(62) Hollebeek, T.; Ho, T.-S.; Rabitz, H. *J. Chem. Phys.* **2001**, *114*, 3940.
(63) Brooks, B. R.; Bruccoleri, R. E.; Olafson, B. D.; States, D. J.; Swaminathan, S.; Karplus, M. *J. Comput. Chem.* **1983**, *4*, 187.
(64) Allinger, N. L.; Yuh, Y. H.; Lii, J. H. *J. Am. Chem. Soc.* **1989**, *111*, 8551.
(65) Lii, J. H.; Allinger, N. L. *J. Am. Chem. Soc.* **1989**, *111*, 8566.
(66) Lii, J. H.; Allinger, N. L. *J. Am. Chem. Soc.* **1989**, *111*, 8576.
(67) Pearlman, D. A.; Case, D. A.; Caldwell, J. W.; Ross, W. S.; Cheatham, T. E.; III; DeBolt, S.; Ferguson, D.; Seibel, G.; Kollman, P. *Comput. Phys. Commun.* **1995**, *91*, 1.
(68) Halgren, T. A. *J. Comput. Chem.* **1996**, *17*, 490.
(69) London, F. *Z. Electrochem.* **1929**, *35*, 552.
(70) Ellison, F. O. *J. Am. Chem. Soc.* **1963**, *85*, 3540.
(71) Blais, N. C.; Truhlar, D. G. *J. Chem. Phys.* **1973**, *58*, 1090.
(72) Tully, J. C. In *Semiempirical Methods of Electronic Structure Theory, Part A: Techniques*; Segal, G. A., Ed.; Plenum: New York, 1977; p 173.
(73) Truhlar, D. G.; Wyatt, R. E. *Adv. Chem. Phys.* **1977**, *36*, 141.
(74) Kuntz, P. J. In *Atom-Molecule Collision Theory*; Bernstein, R. B., Ed.; Plenum: New York, 1979; p 79.
(75) Faist, M. B.; Muckerman, J. T. *J. Chem. Phys.* **1979**, *71*, 225.
(76) Vila, C. L.; Kinsey, J. L.; Ross, J.; Schatz, G. C. *J. Chem. Phys.* **1979**, *70*, 2414.
(77) Warshel, A.; Weiss, R. M. *J. Am. Chem. Soc.* **1980**, *102*, 6218.
(78) Zeiri, Y.; Shapiro, M. *J. Chem. Phys.* **1981**, *75*, 1170.
(79) Pross, A.; Shaik, S. S. *Acc. Chem. Res.* **1983**, *16*, 363.
(80) Duggan, J. J.; Grice, R. *J. Chem. Soc., Faraday Trans. 2* **1984**, *80*, 739.
(81) Garrett, B. C.; Truhlar, D. G. *J. Chem. Phys.* **1985**, *82*, 4543.
(82) Sevin, A. *NATO ASI Ser., Ser. C* **1986**, *176*, 235.
(83) Bernardi, F.; McDouall, J. J. W.; Robb, M. A. *J. Comput. Chem.* **1987**, *8*, 296.
(84) Bernardi, F.; Olivucci, M.; McDouall, J. J. W.; Robb, M. A. *J. Am. Chem. Soc.* **1987**, *109*, 544.
(85) Warshel, A.; Sussman, F.; Hwang, J. K. *J. Mol. Biol.* **1988**, *201*, 139.
(86) Chang, Y. T.; Miller, W. H. *J. Phys. Chem.* **1990**, *94*, 5884.
(87) Warshel, A. *Computer Modeling of Chemical Reactions in Enzymes and Solutions*; John Wiley & Sons: New York, 1991.
(88) Yadav, A.; Jackson, R. M.; Holbrook, J. J.; Warshel, A. *J. Am. Chem. Soc.* **1991**, *113*, 4800.
(89) Kabbaj, O. K.; Lepetit, M. B.; Malrieu, J. P.; Sini, G.; Hiberty, P. C. *J. Am. Chem. Soc.* **1991**, *113*, 5619.
(90) Cimiraglia, R. *NATO ASI Ser., Ser. B* **1992**, *299*, 11.
(91) Chang, Y. T.; Minichino, C.; Miller, W. H. *J. Chem. Phys.* **1992**, *96*, 4341.
(92) Benneyworth, P. R.; Balint-Kurti, G. G.; Davis, M. J.; Williams, I. H. *J. Phys. Chem.* **1992**, *96*, 4346.
(93) Aaqvist, J.; Warshel, A. *Chem. Rev.* **1993**, *93*, 2523.
(94) Shaik, S.; Reddy, A. C. *J. Chem. Soc., Faraday Trans.* **1994**, *90*, 1631.
(95) Mathis, J. R.; Bianco, R.; Hynes, J. T. *J. Mol. Liq.* **1994**, *61*, 81.
(96) Kong, Y. S.; Warshel, A. *J. Am. Chem. Soc.* **1995**, *117*, 6234.
(97) Mestres, J.; Hiberty, P. C. *New J. Chem.* **1996**, *20*, 1213.
(98) Aaqvist, J. In *Computational Approaches to Biochemical Reactivity*; Naray-Szabo, G.; Warshel, A., Eds.; Kluwer Academic: Dordrecht, 1997; Vol. 19; p 341.
(99) Allison, T. C.; Mielke, S. L.; Schwenke, D. W.; Truhlar, D. G. *J. Chem. Soc., Faraday Trans.* **1997**, *93*, 825.
(100) Minichino, C.; Voth, G. A. *J. Phys. Chem. B* **1997**, *101*, 4544.
(101) Cattaneo, P.; Persico, M. *Chem. Phys.* **1997**, *214*, 49.
(102) Bottoni, A. *J. Phys. Chem. A* **1998**, *102*, 10 142.
(103) Dobrovsky, I.; Levine, R. D. *Chem. Phys. Lett.* **1998**, *286*, 155.
(104) Kolmodin, K.; Hansson, T.; Danielsson, J.; Aqvist, J. *ACS Symp. Ser.* **1999**, *721*, 370.
(105) Anglada, J. M.; Besalu, E.; Bofill, J. M.; Crehuet, R. *J. Comput. Chem.* **1999**, *20*, 1112.
(106) Anglada, J. M.; Besalu, E.; Bofill, J. M.; Crehuet, R. *J. Comput. Chem.* **1999**, *20*, 1130.
(107) Mo, Y.; Gao, J. *J. Phys. Chem. A* **2000**, *104*, 3012.
(108) Garrett, B. C.; Truhlar, D. G. *J. Phys. Chem.* **1979**, *83*, 2921.
(109) Garrett, B. C.; Truhlar, D. G. *J. Phys. Chem.* **1979**, *83*, 1079.
(110) Garrett, B. C.; Truhlar, D. G. *J. Am. Chem. Soc.* **1979**, *101*, 4534.
(111) Garrett, B. C.; Truhlar, D. G.; Grev, R. S.; Magnuson, A. W. *J. Phys. Chem.* **1980**, *84*, 1730.
(112) Truhlar, D. G.; Garrett, B. C. *Acc. Chem. Res.* **1980**, *13*, 440.
(113) Isaacson, A. D.; Truhlar, D. G. *J. Chem. Phys.* **1982**, *76*, 1380.
(114) Allison, T. C.; Truhlar, D. G. In *Modern Methods for Multidimensional Dynamics Computations in Chemistry*; Thompson, D. L., Ed.; World Scientific: Singapore, 1998; p 618.
(115) Nguyen, K. A.; Jackels, C. F.; Truhlar, D. G. *J. Chem. Phys.* **1996**, *104*, 6491.
(116) Chuang, Y.-Y.; Truhlar, D. G. *J. Phys. Chem. A* **1998**, *102*, 242.
(117) Downing, J. W.; Michl, J. In *Potential Energy Surfaces and Dynamics Calculations*; Truhlar, D. G., Ed.; Plenum: New York, 1981; p 199.
(118) Chen, Z. *Theor. Chim. Acta* **1989**, *75*, 481.
(119) Corchado, J. C.; Kim, Y.; Villa, J.; Albu, T. V.; Xing, J.; Truhlar, D. G. TINKERATE 8.5 University of Minnesota, Minneapolis, 2000.
(120) Corchado, J. C.; Chuang, Y.-Y.; Fast, P. L.; Villà, J.; Hu, W.-P.; Liu, Y.-P.; Lynch, G. C.; Nguyen, K. A.; Jackels, C. F.; Melissas, V. S.; Lynch, B. J.; Rossi, I.; Coitiño, E. L.; Fernandez-Ramos, A.; Steckler, R.; Garrett, B. C.; Isaacson, A. D.; Truhlar, D. G. POLYRATE 8.5.1 University of Minnesota, Minneapolis, 2000.
(121) Ponder, J. W. TINKER 3.5 Washington University, St. Louis, MO, 1997.
(122) Corchado, J. C.; Chuang, Y.-Y.; Coitiño, E. L.; Truhlar, D. G. GAUSSRATE 8.6 University of Minnesota, Minneapolis, 2000.
(123) Frisch, M. J.; Trucks, G. W.; Schlegel, H. B.; Scuseria, G. E.; Robb, M. A.; Cheeseman, J. R.; Zakrzewski, V. G.; Montgomery, J. A.; Stratmann, R. E.; Burant, J. C.; Dapprich, S.; Millam, J. M.; Daniels, A. D.; Kudin, K. N.; Strain, M. C.; Farkas, O.; Tomasi, J.; Barone, V.; Cossi, M.; Cammi, R.; Mennucci, B.; Pomelli, C.; Adamo, C.; Clifford, S.; Ochterski, J.; Petersson, G. A.; Ayala, P. Y.; Cui, Q.; Morokuma, K.; Malick, D. K.; Rabuck, A. D.; Raghavachari, K.; Foresman, J. B.; Cioslowski, J.; Ortiz, J. V.; Stefanov, B. B.; Liu, G.; Liashenko, A.; Piskorz, P.; Komaromi, I.; Gomperts, R.; Martin, R. L.; Fox, D. J.; Keith, T.; Al-Laham, M. A.; Peng, C. Y.; Nanayakkara, A.; Gonzalez, C.; Challacombe, M.; Gill, P. M. W.; Johnson, B. G.; Chen, W.; Wong, M. W.; Andres, J. L.; Head-Gordon, M.; Replogle, E. S.; Pople, J. A. *Gaussian98 (Revision A.9)*; Gaussian, Inc.: Pittsburgh, PA, 1998.
(124) Page, M.; McIver, J. W., Jr. *J. Chem. Phys.* **1988**, *88*, 922.
(125) Chuang, Y.-Y.; Truhlar, D. G. *J. Chem. Phys.* **2000**, *112*, 1221.
(126) Glasstone, S.; Laidler, K.; Eyring, H. *The Theory of Rate Processes*; McGraw-Hill: New York, 1941.

(127) Cohen, N.; Westberg, K. R. *Int. J. Chem. Kinet.* **1986**, *18*, 99.
(128) Cohen, N. *Int. J. Chem. Kinet.* **1986**, *18*, 59.
(129) Sutherland, J. W.; Michael, J. V.; Klemm, R. B. *J. Phys. Chem.* **1986**, *90*, 5941.
(130) Herron, J. T. *J. Phys. Chem. Ref. Data* **1988**, *17*, 967.
(131) Baulch, D. L.; Cobos, C. J.; Cox, R. A.; Esser, C.; Frank, P.; Just, T.; Kerr, J. A.; Pilling, M. J.; Troe, J. *J. Phys. Chem. Ref. Data* **1992**, *21*, 411.
(132) Clary, D. C. *Phys. Chem. Chem. Phys.* **1999**, *1*, 1173.
(133) Roberto-Neto, O.; Machado, F. B. C.; Truhlar, D. G. *J. Chem. Phys.* **1999**, *111*, 10 046.
(134) Bersuker, I. B. *The Jahn−Teller Effect and Vibronic Interactions in Modern Chemistry*; Plenum Press: New York, 1984.
(135) Gonzalez, C.; McDouall, J. J. W.; Schlegel, H. B. *J. Phys. Chem.* **1990**, *94*, 7467.
(136) Espinosa-Garcia, J.; Garcia-Bernaldez, J. C. *Phys. Chem. Chem. Phys.* **2000**, *2*, 2345.
(137) Truong, T. N.; Truhlar, D. G. *J. Chem. Phys.* **1990**, *93*, 1761.
(138) Melissas, V. S.; Truhlar, D. G. *J. Chem. Phys.* **1993**, *99*, 3542.
(139) Chuang, Y.-Y.; Corchado, J. C.; Truhlar, D. G. *J. Phys. Chem. A* **1999**, *103*, 1140.
(140) Espinosa-Garcia, J.; Corchado, J. C. *J. Chem. Phys.* **2000**, *112*, 5731.
(141) Masgrau, L.; Gonzalez-Lafont, A.; Lluch, J. M. *J. Chem. Phys.* **2001**, *114*, 2154.
(142) *CRC Handbook of Chemistry and Physics*, 75th ed.; Lide, D. R., Ed.; CRC Press: Boca Raton, FL, 1994.